JOHANNES KEPLER
UNIVERSITY LINZ

Submitted by
David Doppelbauer

Submitted at
Institute of Semiconductor and Solid State Physics

Supervisor
Prof. Dr. Andreas Ney

2nd Supervisor
Dr. Philipp Stadler

Co-Supervisor
Dr.in Verena Ney

February 2020

$ZnCo_2O_4$ as (Photo-) Electrocatalyst for the Oxygen Evolution Reaction

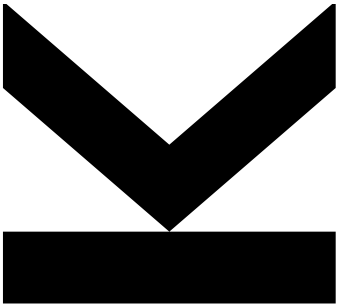

Master Thesis
to obtain the academic degree of
Diplom-Ingenieur
in the Master's Program
Technische Physik

JOHANNES KEPLER UNIVERSITY LINZ
Altenbergerstraße 69
4040 Linz, Österreich
www.jku.at
DVR 0093696

Eidesstattliche Erklärung

Ich erkläre an Eides statt, dass ich die vorliegende Masterarbeit selbstständig und ohne fremde Hilfe verfasst, andere als die angegebenen Quellen und Hilfsmittel nicht benutzt bzw. die wörtlich oder sinngemäß entnommenen Stellen als solche kenntlich gemacht habe.
Die vorliegende Masterarbeit ist mit dem elektronisch übermittelten Textdokument identisch.

_____

David Doppelbauer, B.Sc.

Abstract

In this thesis, the electro- and photoelectrocatalytical properties for the oxygen evolution reaction of $ZnCo_2O_4$ have been investigated. p-type $ZnCo_2O_4$, grown on a Titanium mesh substrate, is used for electrochemistry measurements in a conventional H-cell with potassium hydroxide aqueous solution. In order to study the catalysis under illumination with sun light (solar simulator, $100\,\mathrm{mW/cm^2}$) in a flow cell, the $ZnCo_2O_4$ is grown on a transparent and conducting 2%Al:ZnO layer. In this case, a c-sapphire substrate is used. The structures are fabricated in an ultra high vacuum chamber by reactive magnetron sputtering and/or pulsed laser deposition. The crystal structure of the grown samples is characterized by x-ray diffraction and the chemical composition is analyzed by x-ray photoelectron spectroscopy and Auger electron spectroscopy. The electrochemical experiments show that $ZnCo_2O_4$ is an efficient catalyst for the oxygen evolution reaction, exhibiting overpotentials in the range of 390–470 mV and Tafel slopes of 56–103 mV/dec in potassium hydroxide. Long-term stability tests demonstrate performance over several hundreds of hours. Furthermore, first photoelectrochemical measurements with the solar simulator in a working flow cell have been done. However, 2%Al:ZnO is unstable in potassium hydroxide aqueous solution, strongly affecting the stability of the system, even when the samples are capped with gold layers.

Keywords: Electrocatalysis, Photoelectrocatalysis, OER, Semiconductor, $ZnCo_2O_4$, ZnO, Oxides

Zusammenfassung

Im Zuge dieser Masterarbeit werden die elektro- und photoelektrokatalytischen Eigenschaften von $ZnCo_2O_4$ zur Sauerstofferzeugung untersucht. Dazu wird p-Typ $ZnCo_2O_4$ gewachsen auf ein Titan-Netz Substrat gewachsen und in einer gewöhnlichen H-Zelle mit Kaliumhydroxid wässriger Lösung verwendet. Um die Katalyse bei Beleuchtung mit Sonnenlicht (Solarsimulator, $100\,{}^{\mathrm{mW}}/_{\mathrm{cm}^2}$) in einer Flow-Zelle zu studieren, wird $ZnCo_2O_4$ auf einer transparenten und leitfähigen 2%Al:ZnO Schicht gewachsen. In diesem Fall dient c-Saphir als Substrat. Die Strukturen werden in einer Ultrahochvakuum Kammer durch reaktives Magnetronsputtern und/oder durch gepulste Laserdeposition hergestellt. Die Kristallstruktur der gewachsenen Proben wird durch Röntgenbeugung charakterisiert, die chemische Zusammensetzung durch Röntgenphotoelektronenspektroskopie und Augerelektronenspektroskopie untersucht. Die Experimente zeigen, dass $ZnCo_2O_4$ ein effizienter Katalysator für die Sauerstofferzeugung ist. $ZnCo_2O_4$ weist Überpotentiale im Bereich von 390–470 mV und Tafel Steigungen von 56–103 mV/dec in Kaliumhydroxid auf. Langzeit-Stabilitätstests demonstrieren die Funktion über mehrere hundert Stunden. Außerdem werden erste photoelektrochemische Experimente in einer Flow-Zelle durchgeführt. Jedoch beeinträchtigt die Instabilität von 2%Al:ZnO in Kaliumhydroxid wässriger Lösung die Stabilität des Systems enorm, auch wenn die Proben mit einer Schutzschicht aus Gold bedeckt werden.

Stichwörter: Elektrokatalyse, Photoelektrokatalyse, OER, Halbleiter, $ZnCo_2O_4$, ZnO, Oxide

Table of Contents

Nomenclature

Latin Letters

Variable	Denotation	Unit
a	In-plane Lattice constant	Å
c	Out-of-plane lattice constant	Å
A	Area	m^2
d	Lattice plane spacing	m
E	Electrochemical Potential	V
E^0	Standard Potential	V
E_B	Binding energy	eV
E_g	Bandgap energy	eV
$\mathcal{F}$	Fillfactor	–
F	Faraday constant	96485.3 $^{\text{C}}/_{\text{mol}}$
ΔG	Gibbs Free Energy	$^{\text{kJ}}/_{\text{mol}}$
ΔG^0	Standard Gibbs Free Energy	$^{\text{kJ}}/_{\text{mol}}$
$\Delta G^\ddagger$	Gibbs Free Energy of Activation	$^{\text{kJ}}/_{\text{mol}}$
(h,k,l)	Miller indices	–
$\hbar$	Reduced Planck's constant	$6.5821 \cdot 10^{-16}$ eVs
j	Current density	$^{\text{mA}}/_{\text{cm}^2}$
j_0	Exchange current density	$^{\text{mA}}/_{\text{cm}^2}$
k	Wave vector	$^{1}/_{\text{m}}$
M	Molar concentration	$^{\text{mol}}/_{\text{volume}}$
n	Number of electrons	–
p	Pressure	bar
Q_r	Reaction coefficient	–
R	Gas constant	8.3145 $^{\text{J}}/_{\text{mol K}}$
R_S	Sheet Resistance	Ω
T	Temperature	K
T_H	Heater temperature	℃
t	Time	s
$[x]$	Mass concentration	$^{\text{g}}/_{\text{L}}$

Greek Letters

Variable	Denotation	Unit
α	Transfer coefficient	–
ϑ	Angle	$^\circ$
λ	Wavelength	nm
ω	Angular Frequency	$^1/_\mathrm{s}$
ν	Frequency	$^1/_\mathrm{s}$
ρ	Density	$^\mathrm{g}/_{\mathrm{cm}^3}$
ρ_e	Resistivity	$\Omega\,\mathrm{cm}$
η	Overpotential	mV
ϕ	Work function	eV

Abbreviations

Abbreviation	Denotation
AES	Auger Electron Spectroscopy
at%	Atomic percent
AZO	2%Al:ZnO
CE	Counter electrode
CV	Cyclic Voltammetry
FWHM	Full width at half-maximum
HER	Hydrogen Evolution Reaction
IGP	Ion Getter Pump
KOH	Potassium Hydroxide
K_2CO_3	Potassium Carbonate
$KHCO_3$	Potassium Bicarbonate
MFC	Mass Flow Controller
OER	Oxygen Evolution Reaction
PEC	Photoelectrochemistry
PLD	Pulsed Laser Deposition
RE	Reference electrode

Abbreviation	**Denotation**
RMS	Reactive Magnetron Sputtering
rpm	Rounds per minute
sccm	Standard Cubic Centimeters
SEM	Scanning Electron Microscope
SHE	Standard Hydrogen Electrode
TC	Thermocouple
TSP	Titanium Sublimation Pump
UHV	Ultra High Vacuum
WE	Working electrode
XPS	X-Ray Photoelectron Spectroscopy
XRD	X-Ray Diffraction

List of Figures

1 Introduction

With the depletion of fossil fuels, progress of climate change [1] and more and more extreme weather conditions, the need for a more sustainable energy system is rising. Around 80 % of the world's energy demand is covered by fossil fuels [2]. In order to stop the pollution of the earth's atmosphere, sustainable and environmentally-friendlier alternatives are required. (Photo-)electrochemical energy conversion and storage has gained great attention because it enables the efficient splitting of water into hydrogen (H_2) and oxygen (O_2) by electricity and (sun)light [3–7]. These gases offer a variety of applications, especially their re-use in fuel cells.

However, the oxygen evolution reaction is a complex four-electron-step reaction, often hindering the reaction and requiring additional energy [2]. Therefore, in order to drive the reaction efficiently at higher rates, catalysts need to be employed. So far, among the best oxygen evolution reaction catalysts are rare metal oxides, e.g. $IrO_x/SrIrO_3$ [8]. The scarcity and costs of these materials limit the commercial use and thus, earth-abundant transition metal oxide catalysts are far more attractive, for example compounds of nickel, iron and cobalt oxides [2, 9]. In addition to the challenge of finding an active material, stability under operation in alkaline media on a suitable, conducting substrate has to be ensured. In previous research, platin, indium tinn oxide, fluorinated tinn oxide or carbon-based substrates are used which are rather expensive or less conducting than, for instance, titanium[10–12].

$ZnCo_2O_4$ is a very interesting catalyst system. Unique coordination of Zn and Co atoms in its crystal structure make it catalytically more active and an environmentally more friendly alternative to Co_3O_4 [11, 13, 14]. Furthermore, absorption in the visible part of the solar spectrum allows the investigation of the catalysis process under illumination with (sun)light [4].

In this thesis, the electro- and photoelectrocatalytic properties of $ZnCo_2O_4$ are investigated. Electrochemistry and characterization experiments are performed on samples

grown by reactive magnetron sputtering and plused laser deposition. As substrate, Ti-meshes are established. The catalytic performance of a $ZnCo_2O_4$ / Titanium mesh sample system with overpotentials comparable to reported metal oxide catalysts is observed. The stability of the catalyst under continuous operation in high alkaline media and oxidizing conditions is shown for almost 500 hours. For photoelectrochemical measurements a different type of setup - a custom-built flow cell - is developed and used. The flow cell requires a different type of sample with a conducting and transparent substrate, e.g. 2%Al:ZnO. Despite the stability issues of Al:ZnO in potassium hydroxide, first successful test experiments in the flow cell have been conducted.

This work is structured in the following way:
Chapter 2 introduces the basic concepts of catalysis and water splitting via (photo-) electrochemical processes along with the governing half-reactions and electrochemical potentials. Then the fundamentals of analytical techniques, namely x-ray diffraction (XRD), x-ray photoelectron spectroscopy (XPS) and Auger electron spectroscopy (AES) are explained.
Chapter 3 outlines the most important structural, electrical and optical properties of the used materials.
In **Chapter 4** all used experimental methods for sample growth and characterization are presented. At first, the two physical vapor deposition methods are explained, followed by XPS and AES, and finally the electrochemical measurements, for example the setup of the cells and the types of measurements performed.
Chapter 5 deals with the results obtained during this thesis. The catalytic effect of $ZnCo_2O_4$ towards the oxygen evolution reaction (OER) is demonstrated and two measures of efficiency, the overpotential and the Tafel slope are determined. A flow cell type of setup enables measurements under illumination, using a transparent 2%Al:ZnO back-electrode.
Finally, in **Chapter 6** the experimental findings are summarized and a short outlook for further possible work and improvements is given.
The **Appendix** includes the spectral distribution of the solar simulator and a simple C++ code for data reduction.

2

Theoretical Background

In this chapter, the theoretical concepts of (photo-) electrochemical water splitting and electrochemical potentials as well as used techniques for analysis (x-ray diffraction, x-ray and Auger electron spectroscopy) are introduced. At first, a short summary of the basic concept of catalysis will be given.

2.1. (Electro-) Catalysis

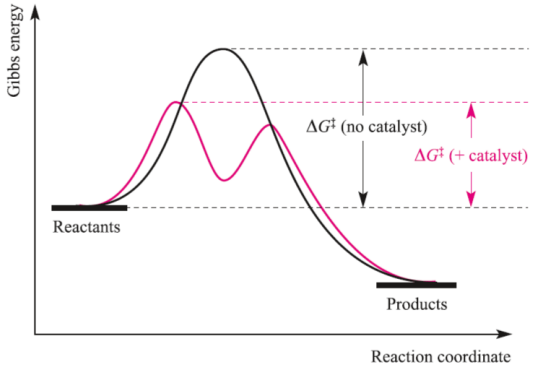

Figure 2.1.: Schematic of a chemical reaction with and without a catalyst. Taken from [15].

Electrocatalysis describes the electron transfer processes in redox reactions. One major topic of this field is studying the change of a chemical reaction by the passage of a current, or its generation by transferring chemical energy into electrical energy by use of a *catalyst* [16]. A catalyst is defined as a substance that speeds up (or slows down) the achievement of equilibrium of a specific reaction without undergoing changes or being consumed [15, 17]. They are classified as homogeneous or heterogeneous, being in the same or a different phase as the participants of the reaction that is catalyzed [15]. The

use of a catalyst allows the reaction to take a different, energetically more favourable path than without it. Consequently, the activation barrier $\Delta G^{\ddagger}$ - the energy barrier that has to be overcome in order for the reaction to take place - is lowered (Fig. 2.1).
As shown, the catalyzed reaction commonly takes place via one or more intermediate steps, but lower activation energy $\Delta G^{\ddagger}$. The rate-determining step is the one with highest activation energy. Catalysts are present in everyday life, for example facilitating the oxidation of carbonmonoxide (CO) to carbondioxide (CO_2) in combustion engines [17]. Nowadays, catalysis focuses on CO_2 reduction [18, 19] and renewable energy, e.g. hydrogen or oxygen evolution by water splitting processes [4, 5, 20, 21].

2.2. (Photo-) Electrochemical Water Splitting

One way of generating renewable and storable energy is the splitting of water (H_2O) into oxygen (O_2) and twice the amount of hydrogen (H_2). The governing reaction is:

$$H_2O + \text{Energy} \longrightarrow O_{2(g)} + 2\ H_{2(g)}, \tag{2.1}$$

where "(g)" stands for the gaseous phase of the reactants. The reaction is thermodynamically unfavourable, requiring external energy of minimum $237.14\,{}^{\mathrm{kJ}}/_{\mathrm{mol}}$ [5].
In alkaline media, the water splitting process is composed of the following half-reactions [3]:

$$\text{Reduction:} \quad 4\ H_2O + 4\ e^- \longrightarrow 2\ H_{2(g)} + 4\ OH^-, \tag{2.2}$$

$$\text{Oxidation:} \quad 4\ OH^- \longrightarrow O_{2(g)} + 2\ H_2O + 4\ e^-, \tag{2.3}$$

the hydrogen (HER) and the oxygen evolution reactions (OER). Water splitting is typically done in an electrochemical cell (Fig. 2.2). In general, it consists of 2 compartments with electrodes dipped in electrolyte, an energy supply and a frit to separate the reactions. Hydrogen and oxygen evolution happens at the cathode and anode, respectively.

When H_2O molecules approach the surface of the cathode and are provided with an electron, hydrogen is adsorbed to the surface - so-called H_{ads} - (Volmer step) and after combining either with a second H_{ads} (Volmer Tafel step) or an H^+ and an e^- (Volmer Heyrovsky step), H_2 and OH^- are formed. The detailed hydrogen evolution mechanism

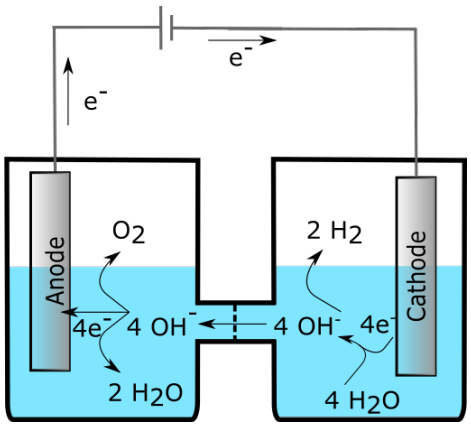

Figure 2.2.: Schematic of the water splitting process.

in alkaline media is [21]:

$$\text{Volmer step:} \quad H_2O + e^- \longrightarrow H_{ads} + OH^-, \tag{2.4}$$

$$\text{Volmer Tafel step:} \quad H_{ads} + H_{ads} \longrightarrow H_2, \tag{2.5}$$

$$\text{Volmer Heyrovsky step:} \quad H^+ + H_{ads} + e^- \longrightarrow H_2. \tag{2.6}$$

The OH^- ions travel through the membrane and are adsorbed at the active sites of the anode. There, it reacts with a second OH^- and 4 e^--transfer steps follow, involving intermediate adsorbed O, OH and OOH species (denoted with "*") to O_2 and water. The details of the steps are still discussed until this day, but the most acknowledged OER mechanism is [21, 22]:

$$* + OH^- \longrightarrow OH^* + e^-, \tag{2.7}$$

$$OH^* + OH^- \longrightarrow O^* + H_2O + e^-, \tag{2.8}$$

$$O^* + OH^- \longrightarrow OOH^* + e^-, \tag{2.9}$$

$$OOH^* + OH^- \longrightarrow * + O_2 + H_2O + e^-. \tag{2.10}$$

Usually, the external energy source is electrical energy, but it is convenient to use - at least partially - renewable energy, e.g. solar energy. This leads to the concept of *photo-electrochemistry*, where light is directly used as an additional source of energy.

If photons (energy $h\nu$) interact with a semiconductor with bandgap E_g lower than

the energy of light, it will be absorbed, creating an electron-hole-pair (Fig. 2.3). The generated photovoltage is added to the external electrical energy and helps to drive the water splitting reaction.

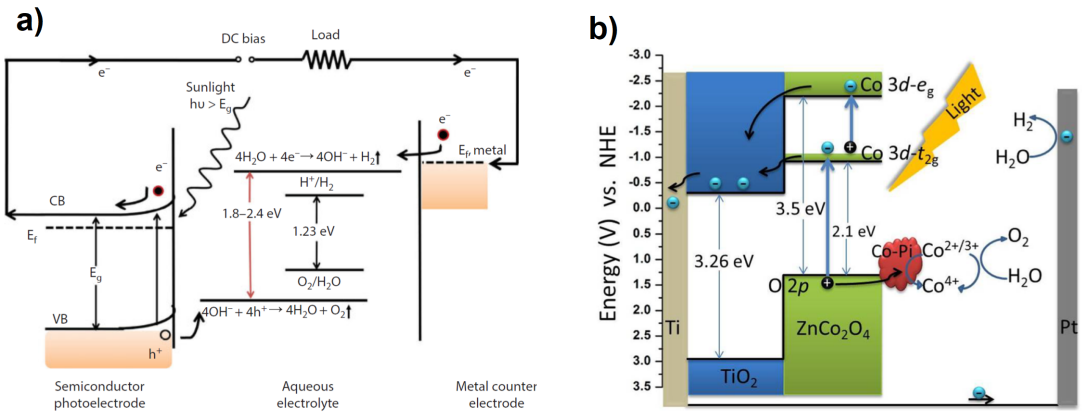

Figure 2.3.: Working principles of photoelectrochemical water splitting [20] (a), and a $ZnCo_2O_4$ photoanode with cobalt phosphate (Co-Pi) nanoparticles [4] (b)

The electron in the conduction band (CB) migrates through the external circuit to the counter electrode, producing hydrogen, and the hole in the valence band (VB) generates oxygen at the anode surface [5]. In Fig. 2.3 a), the semiconductor photoanode is n-type. Therefore, the energy bands at the electrode-electrolyte interface are bent upward. Employing p-type semiconductors as photoelectrodes result in downward band bending [5, 20]. Since downward bending means that the holes will not travel to the catalyst surface easily, they have to be trapped, e.g. with TiO_2 (see Fig. 2.3 b), with low valence band potential [4]. The excited electrons have no problem travelling from the excited states to the platinum (Pt) cathode. Due to the low valence band energy of TiO_2, the holes are much more likely to react with water molecules than to leave the catalyst.

However, the semiconductor of choice must fullfil several conditions. The VB (CB) potential of the electrode must be lower (higher) in order to allow oxygen (hydrogen) evolution reactions. Furthermore, the minimal bandgap energy has to be $E_g \geq 1.229\,\mathrm{eV}$, since $-e \cdot \Delta E^0_{cell} = 1.229\ \mathrm{eV}$ [23], from the standard Gibbs Free Energy of Formation (section 2.3). In order to overcome kinetic barriers and account for electron-transfer losses, bandgaps of $1.6 - 2.4\ \mathrm{eV}$, corresponding to wavelenghts of $500 - 700\ \mathrm{nm}$, are promising, since almost half of the sun radiation lies in this range [3–5, 20]. Further material requirements are stability in the electrolyte, low costs and abundance [2, 8, 14, 21].

2.3. Nernst Equation

In order to gain more insight on the potential of the cell and its relation to the concentration of ions in the half cells, the Nernst equation is considered. It is best explained by considering the reduction reaction:

$$O + ne^- \rightleftharpoons R, \tag{2.11}$$

where R and O are the reduced and oxidized species, respectively, and n the number of electrons taking part in the reaction. The Gibbs Free Energy ΔG of this reaction can be calculated by

$$\Delta G = \Delta G^0 + RT \cdot lnQ_r, \tag{2.12}$$

where $Q_r = \frac{[R]}{[O]}$ is the reaction coeffient. ΔG^0 denotes the Standard Gibbs Free Energy, R the Gas constant (8.3145 $^{\mathrm{J}}/_{\mathrm{mol\ K}}$), T the temperature and [O] and [R] the activity of the oxidized and reduced species, respectively. The superscript in ΔG^0 refers to standard conditions. The resulting potential (difference) across the electrochemical cell E[1] at thermodynamic equilibrium and ΔG can be related via the following equation (with Faraday constant $F = 96485.3\ ^{\mathrm{C}}/_{\mathrm{mol}}$):

$$\Delta G = -nFE \quad \text{or} \quad \Delta G^0 = -nFE^0. \tag{2.13}$$

E^0 is called the *Standard Electrode Potential*. Upon combining equ. 2.12 and 2.13, the *Nernst equation* is obtained [24]:

$$E = E^0 + \frac{RT}{nF} \cdot ln\frac{[O]}{[R]}. \tag{2.14}$$

Considering the reaction 2 H^+ + 2 e^- $\rightleftharpoons$ 2 $H_{2(g)}$ (HER) to Hydrogen gas ($n = 2$), and plugging in into 2.14, one gets

$$E = E^0_{H_2} + \frac{RT}{2F} \cdot ln\ \frac{[H^+]^2}{[H_2]}, \tag{2.15}$$

[1] In electrochemistry, it is common to use E [V] instead of U or V to describe a potential. If E refers to an energy, it will be explicitly mentioned.

and with activity of unity for gases and liquids,

$$E = E^0_{H_2} + \frac{RT}{F} \cdot ln\ [H^+]. \tag{2.16}$$

By converting from natural to decimal logarithm by $ln(x) = 2.303\, log(x)$ and using $log\,[\mathrm{H}^+] = -pH$, the equation reads

$$E = E^0_{\mathrm{H}_2} - \frac{2.303\, RT}{F} \cdot pH \tag{2.17}$$

A similar result is obtained for the Oxygen evolution $2\,\mathrm{H_2O} \rightleftharpoons \mathrm{O_2} + 4\,\mathrm{H}^+ + 4\,\mathrm{e}^-$:

$$E = E^0_{\mathrm{O}_2} - \frac{2.303\, RT}{F} \cdot pH \tag{2.18}$$

The standard potentials of the Hydrogen and Oxygen evolution can be found in the Galvanic Series: $E^0_{\mathrm{H}_2} = 0.0000\ V$ and $E^0_{\mathrm{O}_2} = 1.229\ V$ [25]. The Nernst equation can be visualized by plotting equations 2.17 and 2.18. Fig. 2.4 shows the stability region of water for different pH values (Pourbaix diagram). Line a and b in Fig. 2.4 correspond to the Nernst equation for oxygen and hydrogen, respectively. In between those two lines is the electrochemically stable region of water. The slope of each curve is ≈ -60 mV at room temperature ($T = 298.15\ \mathrm{K}$). This means that the Hydrogen and Oxygen evolution reactions favour lower and higher pH solutions, respectively. The standard potentials of each reaction can be seen at $pH = 0$.

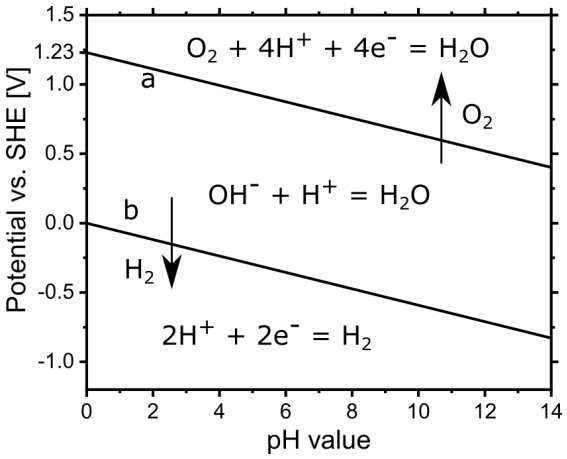

Figure 2.4.: Pourbaix diagram of water. Redrawn from [26].

The potential difference E^0_{cell} of the half reactions is $E^0_{cell} = E^0_{cathode} - E^0_{anode} = -1.229\ \mathrm{V}$. Therefore, the minimum required voltage across the cell for water split-

ting must at least be 1.229 V, or 237.14 $^{\mathrm{kJ}}/_{\mathrm{mol}}$ (equ. 2.13). However, an additional potential is required to overcome kinetic barriers of the oxygen evolution reaction. The rate is strongly limited by the 4-electron processes at the electrode surface in order to generate one O_2 molecule. This excess potential is called *overpotential* η and describes how much is needed in addition to the minimum 1.229 V in order to obtain a certain reaction rate [3, 21, 24, 26]:

$$\eta = E - E^0. \tag{2.19}$$

Naturally, lower overpotentials yield more efficient reactions. Furthermore, a low η means that the system is not driven too far away from its thermodynamic equilibrium. Another measure of efficiency is the *Tafel slope*, which will be explained in the next section.

2.4. Butler-Volmer and Tafel equation

If the reduction reaction $O+ne^- \rightleftharpoons R$ is considered with different reaction rate constants (reactions per time), the Butler-Volmer equation is obtained, which describes the current-overpotential characteristics of electrochemical reactions [24]:

$$j = j_0 \cdot \left(e^{-\frac{\alpha F}{RT} \cdot \eta} - e^{\frac{(1-\alpha)F}{RT} \cdot \eta} \right), \tag{2.20}$$

where j is the current density flowing through the circuit, j_0 the exchange current density, α the transfer coefficient and η the overpotential. The first part of equ. 2.20 describes the cathodic, the second the anodic currents, j_c and j_a, respectively. j_0 is an intrinsic current, even when no net current is flowing at the equilibrium potential E predicted by the Nernst equation. At this (dynamic) equilibrium the overall current density $j = j_c - j_a$ equals zero. Consequently, j_c and j_a, are balanced, and $j_0 = j_c = j_a$. It is important to mention that only one-step and one-electron processes are assumed but mass-transfer limitations from solution to the electrode are excluded. This means that in this case the overpotential stems from overcoming the activation barrier of the reaction. Practically, mass transfer limitations can be reduced by stirring the solution.

For large positive or negative overpotentials η, the cathodic or the anodic part is way smaller than the other, respectively. Assuming $\eta >> 1$ (high positive overpotentials), equ. 2.20 reduces to

$$j = -j_0 \cdot e^{\frac{(1-\alpha)F}{RT}\ \eta}, \tag{2.21}$$

By rearranging, the *Tafel equation* for anodic overpotentials is calculated to:

$$\eta = -\frac{RT\ lnj_0}{(1-\alpha)F} + \frac{2.303\,RT}{(1-\alpha)F}\ logj. \tag{2.22}$$

Equ. 2.22 links the overpotential to the logarithm of the resulting current. By plotting η vs. the logarithm of j, the Tafel slope can be determined by fitting the linear part of equ. 2.20, which is a measure of the reaction kinetics. This *Tafel plot* also allows the calculation of j_0 and α. Moreoever, the slope can be used to determine the rate-determining step of equ. 2.7–2.10. This is the step which influences the reaction rate (proportional to the produced current) the most. Depending on this rate-determining step, Tafel slopes of $21\ {}^{\mathrm{mV}}/_{\mathrm{dec}} - 120\ {}^{\mathrm{mV}}/_{\mathrm{dec}}$ have been theoretically predicted [27]. The surface adsorbed O, OH, OOH species (with different coverages on the electrode surface) are considered in order to simulate the Tafel plots, where each of equations 2.7–2.10 is assumed to be the rate-determining step once. However, the simulations represent the ideal case without further reaction limitations and/or ohmic losses which means that the calculated slopes are an estimation of the lowest theoretical values. Therefore, in real systems, higher Tafel slopes are observed [10–13, 21, 28]. Lower Tafel slopes mean a more efficient catalyst, since the required overpotential to increase the current by a decade is small [3, 24]. The Tafel equation is valid when $|\eta| > 118\ \mathrm{mV}$ at room temperature, and if mass-transfer limitations can be excluded. Otherwise, if electron transfer processes are fast compared to mass transfer, the Tafel equation is not suitable. However, if slow electrode kinetics are present with high overpotentials, good agreement with the Tafel equation can be established [16].

2.5. Reference electrodes

In order to set a reference point for electrochemical potentials, the hydrogen evolution reaction (in acidic environment) is used: $2\ H^+ + 2\ e^- \rightleftharpoons 2\ H_2$. By convention, the standard potential of this reaction is set to $E^0_{H^+/H_2} \equiv 0.0000$ V at all temperatures, H^+ activity of 1 and 1 atm hydrogen pressure. This zero point of potential is called *Stan-*

dard Hydrogen Electrode (SHE) [29], meaning that equ. 2.17 becomes $E = E^0_{H_2} = 0$ V, if pH $= 0$. Thus, the standard potentials of the hydrogen and oxygen evolution reactions are: $E^0_{H_2} = 0$ V, and $E^0_{O_2} = 1.23$ V (as already used above). Usually other reference electrodes are used in measurements, depending on the acidic or alkaline environment, e.g. silver/silver chloride (Ag/AgCl) or mercury/mercuric oxide (Hg/HgO) electrodes [25, 30].

Since the pH value of the used solution has an important effect on the electrochemical potential, the *Reversible Hydrogen Electrode* (RHE) potential must be utilized. It is also based on the SHE, but measured potentials are independent of the pH of the solution [3]. The zero point is shifted by $-\frac{2.303RT}{F}$ pH vs. SHE in order to eliminate the pH-dependency of equations 2.17 and 2.18. Therefore, the potential vs. RHE is:

$$E \text{ vs. RHE} = E^0_{H_2} + \frac{2.303\,RT}{F} \cdot pH \tag{2.23}$$

The advantage of the RHE is, that it makes the comparison of measurements possible, even if they were done in different solutions.

In this thesis, a 1 molar KOH Hg/HgO reference electrode is used, with standard potential $E^0_{Hg/HgO}$ vs. SHE. The potential relation of SHE, RHE and Hg/HgO electrode are sketched in Fig. 2.5.

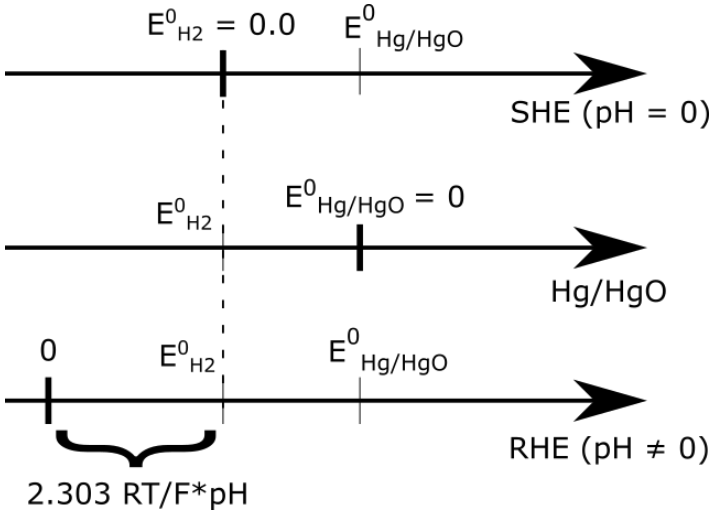

Figure 2.5.: Position of reference potentials (zero points in bold). $E^0_{H_2} = 0$ V vs. SHE per definition.

By convention, $E^0_{H_2} \equiv 0.0000$ V vs. SHE at pH $= 0$. If a voltage E is applied vs. the Hg/HgO electrode, the zero point of the measurement is 0 V vs. Hg/HgO and therefore a potential $E_{Hg/HgO}$ (vs. Hg/HgO) $= E^0_{Hg/HgO} + E$ vs. SHE. Similarly, the applied

potential vs. an arbitrary reference elctrode is converted to potentials vs. RHE via the following relation, for any pH:

$$E \text{ vs. RHE} = E^0_{\text{ref}} + E_{\text{ref}} + \frac{2.303\,RT}{F} \cdot pH, \tag{2.24}$$

where E_{ref} is the potential that is being applied vs. the reference electrode used.

2.6. X-Ray Diffraction (XRD)

X-ray diffraction is used to study the crystal properties of the used materials. This section gives a short overview of diffraction processes.

If a monochromatic, plane wave with wavelength λ (wave vector $\mathbf{k_i}$ or angular frequency ω) impinges on a resting point charge, it will start to oscillate. Since an oscillation means acceleration, dipole radiation will be emitted in form of an electromagnetic wave. If the observer is far away, it is a spherical wave with wave vector $\mathbf{k_f}$, and a deflection of 2θ with respect to the incoming wave. If only elastic scattering is considered, equation 2.25 holds [31]:

$$k_i = k_f = k = \frac{2\pi}{\lambda}, \qquad \text{with} \tag{2.25}$$

$$k = \frac{\omega}{c} \qquad \text{where c} \ldots \text{speed of light} \tag{2.26}$$

In a perfect crystal, electrons are present with a density of $\rho(\mathbf{r}) = \rho(\mathbf{r} + \mathbf{R})$, because of the translation invariance by a lattice vector $\mathbf{R}$. Thus, it can be expressed as a Fourier series

$$\rho(\mathbf{r}) = \sum_{\mathbf{G}} \rho_{\mathbf{G}} e^{i\mathbf{G}\cdot\mathbf{r}}, \tag{2.27}$$

where $\rho_{\mathbf{G}}$ is the Fourier coefficient and $\mathbf{G}$ a reciprocal lattice vector, defined by

$$\mathbf{G} \cdot \mathbf{R} = 2\pi \cdot n, \qquad \text{n} = \text{integer}. \tag{2.28}$$

Following these calculations, the scattered intensity can be written as follows:

$$I(\mathbf{Q}) \propto \left| \sum_{\mathbf{G}} \rho_{\mathbf{G}}\ \delta(\mathbf{Q} - \mathbf{G}) \right|^2. \tag{2.29}$$

$\mathbf{Q} = \mathbf{k}_f - \mathbf{k}_i$ is the momentum transfer, also called scattering vector. From equ. 2.29, it can be seen that scattering only occurs in special directions, when the momentum transfer $\mathbf{Q}$ equals the reciprocal lattice vector $\mathbf{G}$. This is the so-called Laue-condition:

$$\mathbf{Q} = \mathbf{k}_f - \mathbf{k}_i = \mathbf{G}, \tag{2.30}$$

which is equivalent to the Bragg equation:

$$2\ d_{hkl}\ sin(\theta) = n\ \lambda. \tag{2.31}$$

Whenever equation 2.31, with spacing d_{hkl} of the lattice plane (hkl), x-ray incidence angle θ, wavelength λ and integer n, is fulfilled, diffraction is allowed and constructive interference of the scattered beam occurs. The full-width at half-maximum of a detected peak is an indication of the crystalline quality of the sample. A narrow FWHM indicates a single crystal, whereas a broadened peak hints to a broader distribution of lattice constants [32].
Using coplanar scattering geometry, for a cubic lattice, the (out-of-plane) lattice parameter c is calculated by

$$c = \frac{\sqrt{h^2 + k^2 + l^2}\ n\ \lambda}{2\ sin(\theta)}, \tag{2.32}$$

whereas for a hexagonal lattice [33], if $h = k = 0$ and $l \neq 0$, c can be determined by

$$c = \frac{n\ l\ \lambda}{2\ sin(\theta)}. \tag{2.33}$$

2.7. X-Ray Photoelectron Spectroscopy (XPS) & Auger Electon Spectroscopy (AES)

The chemical composition of a grown film is interesting, as well. X-ray photoelectron spectroscopy can give information about the chemical state and composition of the surface atoms. Auger electron spectroscopy is similar, a beam of primary electrons is used to ionize secondary electrons from the sample, starting the Auger process. In a good approximation, XPS can be described in a three-step model (Fig. 2.6 a):

1. An x-ray photon hits the sample and excites an electron with binding energy $-|E_\mathrm{B}|$.
2. The ionized electron reaches the surface.
3. It overcomes the work function ϕ_S of the sample, escapes the solid with kinetic energy E_k and is detected by an energy-resolving detector (work function ϕ_sp) [34].

The electron leaves the sample with a kinetic energy $E_\mathrm{k} = \hbar\omega - \phi_\mathrm{S} - |E_\mathrm{B}|$, whereas the kinetic energy measured by the detector is

$$E_\mathrm{k} = \hbar\omega - |E_\mathrm{B}| - \phi_\mathrm{S} - (\phi_\mathrm{sp} - \phi_\mathrm{S}) = \hbar\omega - |E_\mathrm{B}| - \phi_\mathrm{sp}. \tag{2.34}$$

The work function of the sample cancels and therefore, when measuring E_k and knowing ϕ_sp, the binding energies of the emitted electrons can be calculated by $-|E_\mathrm{B}| = E_\mathrm{k} - \hbar\omega + \phi_\mathrm{sp}$.

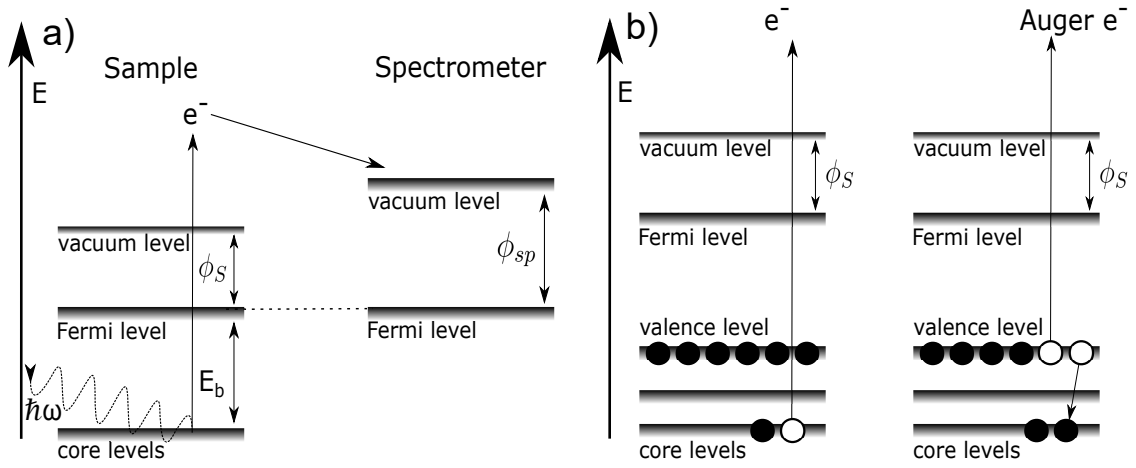

Figure 2.6.: Illustrations of the photoexcitation (a), redrawn from [35], and of the Auger process (b), redrawn and adapted from [36].

Typically, the absolute binding energies are not of interest, but their change in position due to the chemical surrounding of the atom or molecule, the *chemical shift* [34]. The difference in binding energy of an electronic state between a metal and the corresponding metal oxide can give information of the chemical state of an atom.
In order to return to its ground state, the atom or molecule can emit radiation or an electron, previously occupying a higher energy state, fills the empty state [36]. In order to fulfill the law of energy conservation, these electrons have to either give off characteristic x-ray radiation or start the Auger process and eject another elecron, the *Auger electron* (Fig. 2.6 b). Its kinetic energy E_k can be calculated as the difference of the energy of the inital core state and the energy of the other two electrons involved in the process. This technique is called Auger electron spectroscopy.

3
Zinc oxides

Zinc oxide (ZnO) is a transparent II-VI n-type semiconductor with a direct and large bandgap of $\sim 3.3\,\mathrm{eV}$ [37]. Typically, it crystallizes in the hexagonal wurtzite crystal structure with the lattice parameters $a \simeq 3.25\,\text{Å}$ and $c \simeq 5.21\,\text{Å}$ [37]. The electrical properties of ZnO systems open the door for a variety of applications in (opto-) electronics, for example light emitting diodes in the ultraviolet range, photodiodes or transparent transistors [37]. Furthermore, Co doped ZnO (Co:ZnO) compounds exhibit interesting magnetic phenomenons like a vertical exchange-bias effect and uncompensated antiferromagnetism [38, 39]. X-ray absorption spectroscopy measurements reveal that the Cobalt is incorporated on Zn the lattice sites with a valence of $2+$ [38]. When doped with group III metal dopants, e.g. Al:ZnO, a conducting *and* highly transparent material is formed [40]. The Zn-Co-O system used in this thesis is the p-conducting $ZnCo_2O_4$ spinel [41]. $ZnCo_2O_4$ finds applications in Lithium ion batteries as anode materials [42], supercapacitors [43], solar cells [44], and in (photo-) electrochemistry as electrodes for the CO_2 reduction [18, 19] and oxygen evolution reactions [4, 11].
The structural and optical properties of ZnO-based materials are summarized in the following sections.

3.1. 2%Al:ZnO ("AZO")

Doped ZnO, for example with Indium, Gallium or Aluminum, has been reported to be both conducting and transparent. For a 2%Al:ZnO (AZO) film with 500 nm thickness, a resistivity of $4.5 \cdot 10^{-4}\ \Omega\ \mathrm{cm}$ and a transmittance of around 88 % have been demonstrated [45].
Measured sheet resistances of grown samples R_S of a film with a nominal thickness t of 300 nm are around $R_S = 35\,\Omega$ which results in a resistivity of $\rho_e = R_S \cdot t \simeq 10^{-3}\,\Omega\,\mathrm{cm}$.

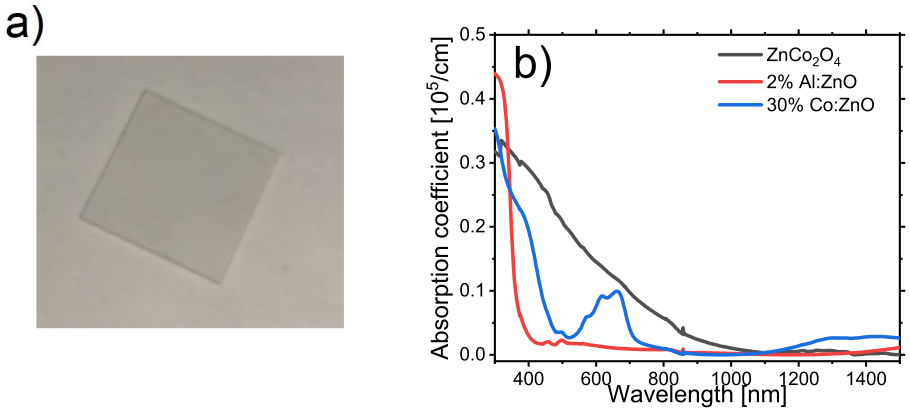

Figure 3.1.: Picture of an AZO sample (a) and optical measurements of $ZnCo_2O_4$, 2%Al:ZnO and 30%Co:ZnO (b) (adapted from [44]).

AZO exhibits metal-like behaviour with a carrier density of $n \cong 3 \cdot 10^{20}\,{}^{1}/_{\mathrm{cm}^3}$, independent of temperature. The carrier mobility slightly decreases with temperature and is around $22\,{}^{\mathrm{cm}^2}/_{\mathrm{Vs}}$ at 300 K [44].
Concerning optical properties, grown AZO samples and Al_2O_3 substrates are optically hard to tell apart (Fig. 3.1 a). Absorption measurements (Fig 3.1 b) show that AZO is very transparent until around 400 nm, whereas Co:ZnO shows an absorption feature at 600–650 nm, accounting for its green colour and use in solar cells [44].

3.2. $ZnCo_2O_4$

Spinels are materials with the general chemical formula AB_2O_4, where A $= \{$Mg, Ni, Zn,$\dots\}$ and B $= \{$Co, Ni, Cu,$\dots\}$ meaning that there are many different types of spinels. The most common crystal structure is the normal cubic $Fd\bar{3}m$. The lattice parameters of the cubic $ZnCo_2O_4$ spinel are $a = b = c \simeq 8.08$ Å [46]. Typically, the Cobalt atoms are occupying the octahedral lattice sites Co_{Oh} in the formal valence state Co^{3+} (Fig. 3.2). The Zinc is located at tetrahedal sites Zn_{Th} with a valence of Zn^{2+} [41]. The Oxygen atoms sit at the egdes of the octahaedrons/tetrahaedrons. Zn_{Oh} together with anti-site defects is believed to be responsible for the resulting p-conductivity [47–49]. $ZnCo_2O_4$ has a bandgap of around $2.63\,\mathrm{eV}$ [50], resulting in a dark brown appearance of grown films on sapphire. The resistance is around $15\,\mathrm{k}\Omega$ with a mobility below $0.4\,{}^{\mathrm{cm}^2}/_{\mathrm{Vs}}$ and a hole density of around $1.6 \cdot 10^{20}\,{}^{1}/_{\mathrm{cm}^3}$ at room temperature [44], which is comparable

to reported values of $2.81 \cdot 10^{20}\,{}^{1}/_{\mathrm{cm}^3}$ [50]. Concerning magnetic properties of $ZnCo_2O_4$, antiferromagnetism is present due to the superexchange coupling of neighbouring Co atoms [41].

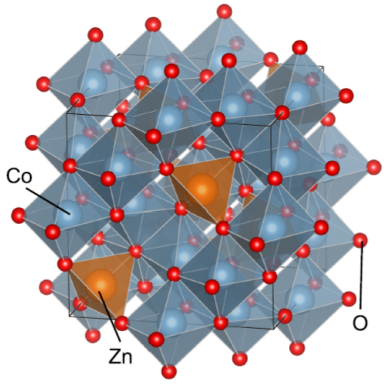

Figure 3.2.: Crystal structure of $ZnCo_2O_4$. Taken from [51].

$ZnCo_2O_4$ is absorbing throughout the visible spectrum (Fig. 3.1 b) and thus a promising material in photoelectrochemical oxygen evolution reactions due to its p-conductivity combined with a bandgap of around $2.63\,\mathrm{eV}$ and absorption properties in the visible range.

The replacement of Co^{2+} by Zn^{2+} atoms in $ZnCo_2O_4$, leaving the Co^{3+} unchanged, results in a slightly better catalytic performance than Co_3O_4, where both oxidation states of Co are present and tetrahedal Co $2+$ sites are not catalytically active [11, 13]. The Zn_{Th} sites have been reported to be inactive with respect to the oxygen evolution, as well. Therefore, $ZnCo_2O_4$ provides a more environmentally-friendly alternative to Cobalt oxides by partly replacing Co with Zn [11].

4

Experimental Methods

4.1. Sample Preparation by RMS & PLD

The samples of this work are prepared using *Reactive Magnetron Sputtering (RMS)* and *Pulsed Laser Deposition* (PLD) which are both Physical Vapor Deposition methods. Both systems are installed in a Ultra High Vaccum (UHV) chamber (Fig. 4.1). The vacuum in the preparation chamber ($p \approx 10^{-9}$ mbar) is achieved by several pumps: a fore-line scroll pump, a turbo pump and an ion getter pump (IGP) with a Titanium sublimation pump (TSP). The pressure is read out by a baratron (minimal pressure $\sim 10^{-5}$ mbar) and an ionisation gauge. The substrates are introduced via a transfer chamber ($p \approx 10^{-8}$ mbar), which is separated from the main chamber by a valve. It is pumped by a rotary vane and a turbo pump. The sample holders are transferred into the preparation chamber by magnetic transfer rods. In addition, the setup consists of an X-Ray Photoelectron Spectroscopy (XPS) chamber ($p \approx 10^{-10}$ mbar).

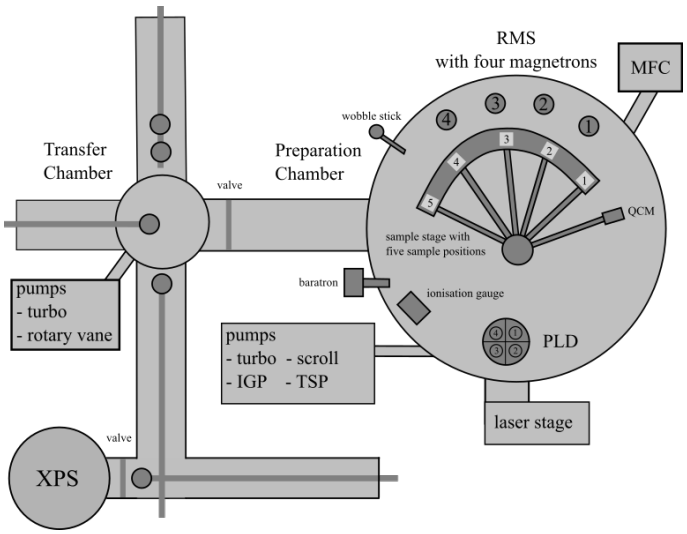

Figure 4.1.: Schematic drawing of the transfer and growth chamber (adapted from [52]).

Usually, the substrate stays in the transfer chamber for at least one day before preparing the film ensuring a sufficient clean environment. When it is brought into the preparation chamber, the holder can be placed on one of five sample positions on the sample stage using a wobble stick. The positions are equipped with different masks, for example $10 \times 10\,\mathrm{mm}^2$ or $7 \times 7\,\mathrm{mm}^2$, which are used in this thesis.

The sample stage can be rotated to the desired magnetron (1–4) on which the target is mounted. In this case, magnetron #3 (Co_3O_4/ZnO) in the RMS and PLD target #1 (Al_2O_3/ZnO) are used. The working pressure of $p \simeq 4 \cdot 10^{-3}\,\mathrm{mbar}$ is achieved by an electronically controlled valve in front of the turbo and the flow of the high-purity Ar and O_2 process gases with mass flow controllers (MFCs). In order to be able to grow $ZnCo_2O_4$ spinels, heaters are placed above the substrates. The maximum achievable temperature is around $850\,°C$. Therefore, the sample is heated from the back because its surface is pointing down towards the magnetron. To ensure correct sample thicknesses, it is important to determine the growth rate. A quartz crystal microbalance (QCM) uses the change of eigen-frequency of the quartz crystal when atoms bond to its surface. This allows the calculation of the growth rate if the density of the material is known. Typical growth rates are around 3–7 $^{\mathrm{nm}}/_{\mathrm{min}}$. Since no literature of the density of the used materials - $ZnCo_2O_4$ and 2%Al:ZnO - could be found, the density of ZnO $\rho = 5.61\,^{\mathrm{g}}/_{\mathrm{cm}^3}$ is taken [53]. The film thickness tends to be lower than the nominal value because of the temperature difference of the water-cooled QCM and the heated sample.

4.1.1. Reactive Magnetron Sputtering

The magnetron for *Reactive Magnetron Sputtering* (RMS) consists of a metal-oxide target with magnets below and a small gas pipe. High voltage ionizes the process gases - creating a plasma - which is then confined by the magnetic field above the target. The accelerated ions sputter the material from the target to the above placed, heated substrate (Fig. 4.2). The $ZnCo_2O_4$ used in this thesis is grown onto a Titanium mesh or AZO/Al_2O_3 substrate from an Co_3O_4/ZnO target with an O_2 : Ar ratio of $10 : 0.5$ sccm, a heater temperature $T_H = 665°C$ and a magnetron power of $30\,\mathrm{W}$. The ideal working pressure is $4 \cdot 10^{-3}$ mbar. The growth parameters have been optimized by B. Henne [41, 51].

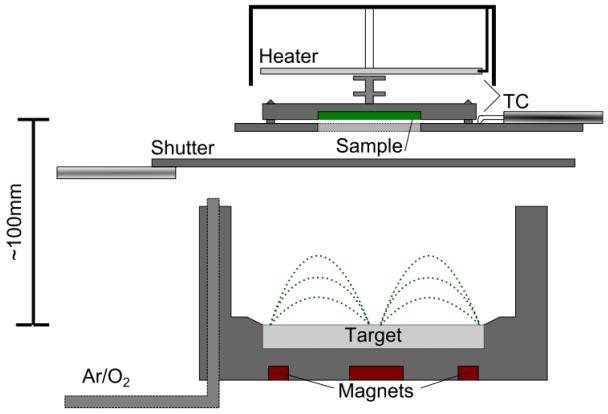

Figure 4.2.: Schematic view of target and sample holder with shutter and the heater. The sample temperature can be read out by thermocouples (TC). Taken from [51]

The colour of a grown $ZnCo_2O_4$ sample on AZO/Al_2O_3 is brown. On a Titanium mesh it looks more violet/blue-ish (see Fig. 4.3).

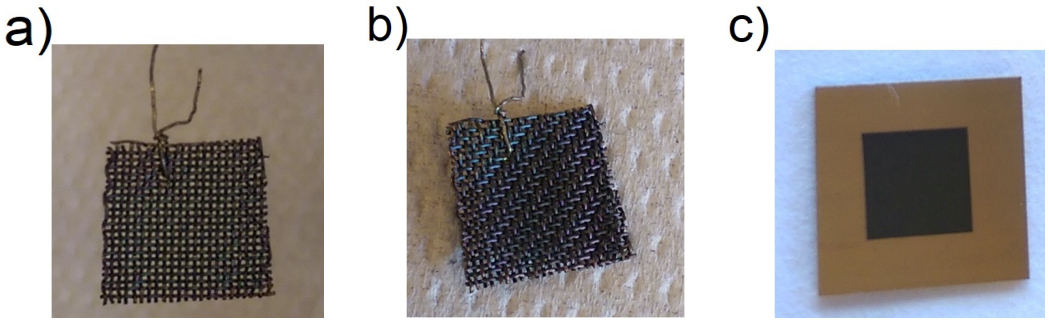

Figure 4.3.: $ZnCo_2O_4$ / Ti-mesh sample (a,b) and $ZnCo_2O_4$ / AZO/ Al_2O_3 sample covered with a 55 nm Au protecting layer on the sides (c).

4.1.2. Pulsed Laser Deposition

The working principle of *Pulsed Laser Deposition* (PLD) is similar to Reactive Magnetron Sputtering. However, in contrast to RMS, the plasma is created by a Q-Smart 850 Nd:YAG laser. The wavelength of 1064 nm is quadrupled to $\lambda = 266\,\mathrm{nm}$. The surface of the material is strongly heated and the atoms evaporated by 100 mJ plasma pulses with a repetition rate of 10 Hz. Two motors ensure the homogeneous ablation of the target by spinning and toggling the target. There are four target positions in the PLD

(Fig. 4.1) which can be removed or exchanged. For instance, 2%Al:ZnO ("AZO") is grown with $T_H = 600°$C and an O_2 : Ar ratio of $10 : 1$ sccm. The chamber pressure is kept at $\sim 4 \cdot 10^{-3}$ mbar, as well. The photograph in Fig. 4.4 shows the transparency of an AZO/ Al_2O_3 sample.

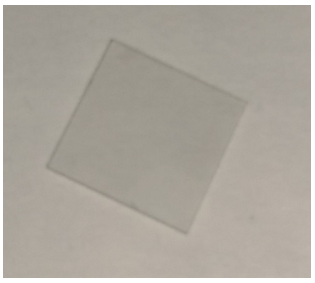

Figure 4.4.: Picture of AZO (#171107) grown with PLD.

4.2. Sample Characterization

4.2.1. X-Ray Diffraction

X-ray diffraction (XRD) measurements are performed in order to get insight into the sample quality, for instance, crystal structure and phase purity, using scattering theory, explained in section 2.6.

An *X'Pert PRO PANalytical MRD Diffractometer* setup is used. The system consists of four main parts: an x-ray tube, beam optics, a sample stage and a detector (Fig. 4.5 a). The x-ray source is a Copper anode, the monochromator either a hybrid two-crystal Germanium (220) Bartels type plus an automatic absorber, or a single graded, parabolic Tungsten/Silicon mirror. Both beam optics are aligned to select the copper $K_{\alpha 1}$-line: $\lambda = 1.5406\,\text{Å}$. The W/Si mirror gives more intensity, whereas the hybrid beam optics gives better resolution but results in lower intensity, since other K_α lines are blocked in contrast to the mirror. In order to avoid detection of the aluminum background from the stage, the samples are glued onto a glass slide with vacuum grease. The XRD spectra are recorded using an acceleration voltage of 40 kV and an electron current to the anode of 40 mA.

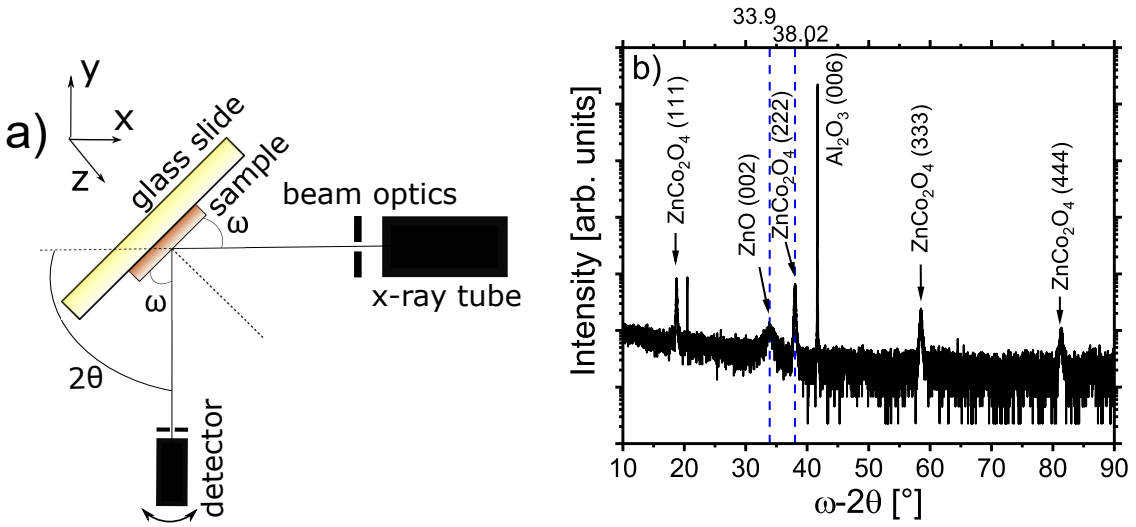

Figure 4.5.: Schematic view of the XRD setup (a) and a typical spectrum of a $2\theta - \omega$ scan (b).

The diffractometer possesses several different scanning methods where parameters like sample angle ω, spatial coordinates or the detector position 2θ are varied and the intensity recorded. For a $2\theta - \omega$ scan, the sample is rotated around the ω-axis and the detector simultaneously moves by an angle of 2θ with twice the drive speed than the sample. This means that in a symmetrical scan θ always equals ω. This is the scan method used to study the sample quality around a known substrate reflection, e.g. the symmetrical Al_2O_3 (006) reflection: $2\theta = 41.68°$ ($\omega = \frac{2\theta}{2} = 20.84°$). One resulting $2\theta - \omega$ scan of $ZnCo_2O_4$ is shown in Fig. 4.5 b). A very narrow substrate peak, ZnO (002) and multiples of the $ZnCo_2O_4$ (111) reflection are visible. When performing an ω-scan, the setup is set to a reflection of either the substrate or the sample and ω is varied. A convenient choice is the before-mentioned (006) peak of the sapphire substrate. This scan is usually performed during the alignment procedure, which is key to a successful measurement. Misalignment results in incorrect positions of the diffraction peaks. Thus, at first, the sample is positioned parallel to the x-ray beam and into its center by iterating ω and the z-position. Secondly, 2θ and ω are set to the sharp and bright (006) substrate peak. Several scans which, for example, align the scattering plane to the sample's surface normal, are performed until the shape and/or position of the peak remain unchanged. Finally, the sample stage is rotated by a given ω and the intensity recorded.

Moreover, the orientation of the lattice planes (mosaicity) can be studied via *rocking scans* by fixing 2θ (the detector) at a certain peak and moving the sample by ω. This

way, the orientation of the set of lattice planes can be examined. If the detected peak is narrow, the planes are parallel [32].

4.2.2. X-Ray Photoelectron Spectroscopy

To investigate the quality of the grown structure further, *X-Ray Photoelectron Spectroscopy* (XPS) measurements are carried out. The technique is based on the photoelectric effect and is often used for chemical analysis because the binding energies E_b of electrons are unique for every element. Moreover, it is surface-sensitive due to the low mean free path of electrons. In principle, it consists of an x-ray gun (Magnesium K_α line: $\hbar\omega = 1253.6\,\mathrm{eV}$), a sample stage and a energy-resolving detector. A molybdenum backplate is placed below the samples, minimizing background signal from the sample holder, possibly consisting of traces of other, previously sputtered materials. After properly warming up the gun for several hours in order minimize thermal drifts in the recorded spectra, the kinetic energy of the detected electrons is recorded and converted to binding energies via $-|E_\mathrm{B}| = E_\mathrm{k} - \hbar\omega + \phi_\mathrm{sp}$.
2 representative scans are shown in Fig. 4.6. Usually, data is plotted as a function of E_b instead of E_k, which means binding energy increases from right to left [35].

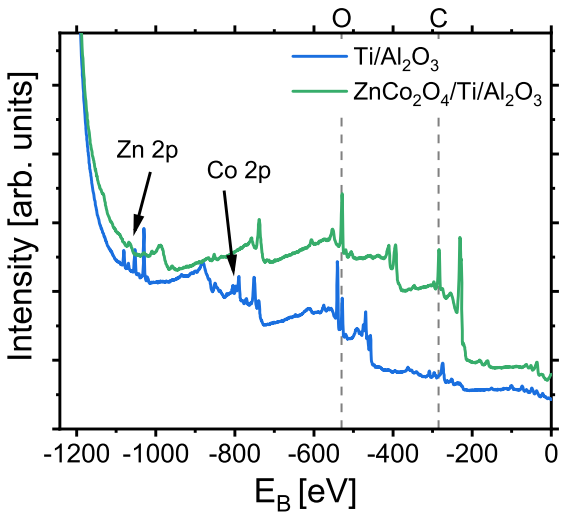

Figure 4.6.: Representative XPS scan of a Ti/Al_2O_3 sample and a $ZnCo_2O_4/Ti$ sample on sapphire.

4.2.3. Auger Electron Spectroscopy

Auger Electron Spectroscopy (AES) is a similar technique but uses the kinetic energy E_k of electrons generated by the Auger process in order to probe the sample surface.

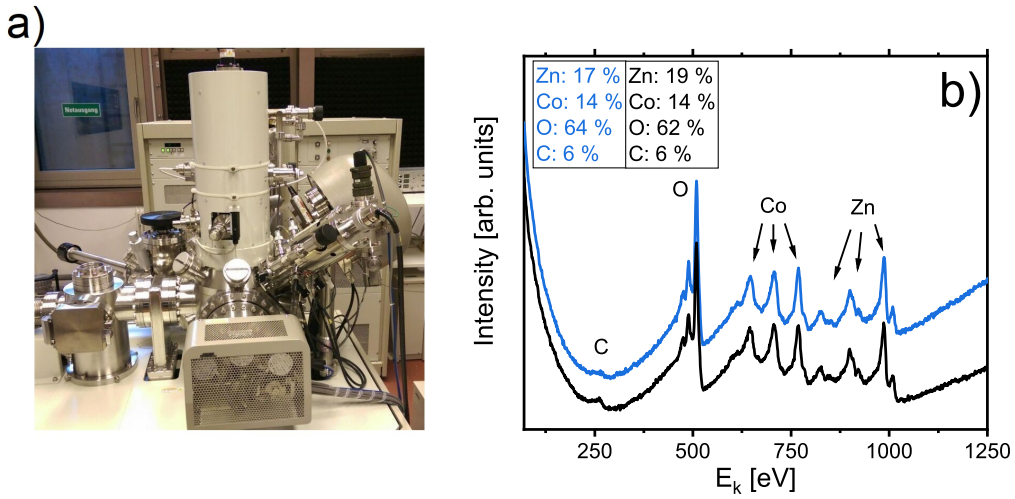

Figure 4.7.: Picture of the used AES setup at the ZONA institute of JKU (a) and a representative scan of a grown $ZnCo_2O_4$ sample (b).

A picture of the setup is shown in Fig. 4.7 a). A beam of electrons is used to excite atoms inside the solid (acceleration voltage: 10 kV). Since these primary electrons can be focused accurately, spacial resolution is higher than in XPS, resulting in a spot size of about $20 - 30\,\mathrm{nm}$. Moreover, the electron beam spot can be controlled precisely. Therefore, different positions on one mesh can be analyzed, e.g. at the middle or the edge of a string. The penetration depth of the primary electrons is around $0.1 - 1\,\mu\mathrm{m}$. Similar to XPS, the recorded kinetic energies E_k of the Auger electrons directly correspond to the electronic states of an atom. However, the mean free path of these electrons is only in the range of a few nanometers. Since only electrons that are able to leave the sample can be detected, AES is even more surface-sensitive than XPS. The background consists of inelastically scattered primary and secondary electrons [35]. A representative plot of a $ZnCo_2O_4$ / Titanium-mesh sample is shown in Fig. 4.7 b). In contrast to XPS, the kinetic energy is the characteristic quantity of the Auger process, no matter if the primary beam consists of ions, x-rays or electrons. Thus, Auger data is usually plotted versus the kinetic energy of the Auger electrons [36].
Since the area under each Auger peak is approximately proportional to the number of atoms in the probed volume, the surface composition in atomic percent (at%) can be

calculated. However, it has to be mentioned that background subtraction has to be carried out and other factors, for example the angle between the beam and detector, the surface geometry of the sample and information depth have to be taken into consideration for exact calculations [35].

4.3. (Photo-)Electrochemistry Measurements

The (photo-) electrocatalytic properties of $ZnCo_2O_4$ are investigated using either an *H-cell* or a *flow cell* configuration of the electrodes for electro- and photoelectrocatalysis measurements, respectively.

4.3.1. Electrochemistry

For a typical investigation of electrocatalytical activities of $ZnCo_2O_4$ a so-called H-cell made of glass is used (Fig. 4.8). It consists of two half cells in which the two half reactions (OER and HER) of water splitting occur. A glass frit is placed between the two cells to slow down diffusion and prevent the formation of dangerous gases, i.e., Oxyhydrogen. Since water has a rather low electrical conductivity, potassium hydroxide (KOH) aqueous solution with a molar concentration of $M = 1\,{}^{\mathrm{mol}}/_{\mathrm{litre}}$ is used as electrolyte. Typical pH values of 1M KOH are around 13.7–14. For better comparison, 1 molar potassium carbonate (K_2CO_3, pH ≈ 12) and potassium bicarbonate ($KHCO_3$, pH ≈ 8) are used, as well. The pH is measured with a *HANNA Instruments pH 211 Microprocessor pH Meter*.

A scheme and a picture of the set-up are shown in Fig. 4.8. The *working electrode (WE)*, the *counter electrode (CE)* and the *reference electrode (RE)* are all connected to a JAISSLE Potentiostat - Galvanostat IMP 88 PC-R or a IVIUM Technologies VERTEX ONE Potentiostat-Galvanostat which provides the voltage with respect to the reference electrode and measures the produced current. The WE is typically the electrode of interest and in this case, responsible for the OER. The CE closes the electrical circuit and performs the HER. In order to minimize voltage drops throughout the circuit (electrolyte, interfaces, membrane,...) a 1M KOH Hg/HgO RE electrode is placed close to the WE. This is called *three-electrode configuration*. It is also possible to use a two-electrode

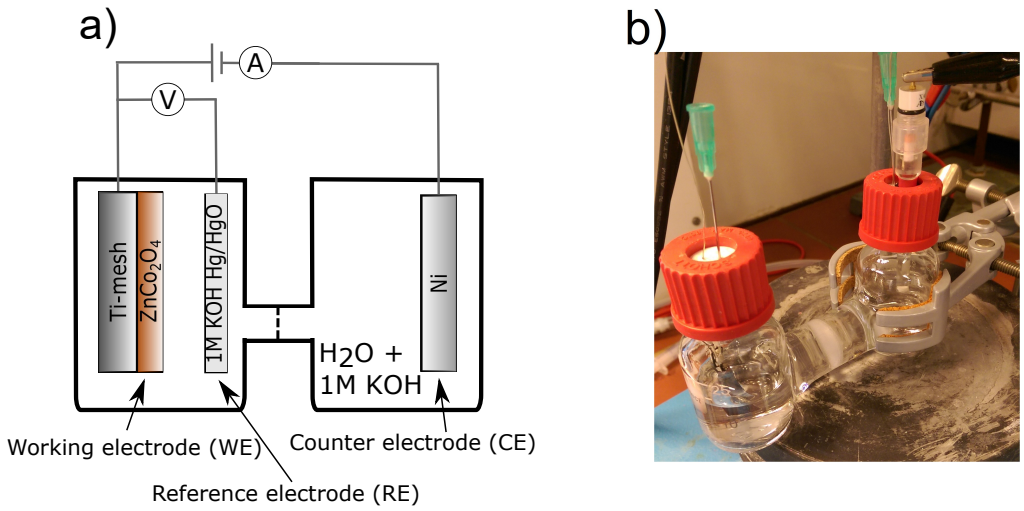

Figure 4.8.: Schematic drawing of the H-cell (a) and a picture taken during a measurement (b).

configuration (by shortcutting WE and RE). However, in this set-up, voltage drops across the membrane and the electrolyte have to be accounted for.

$ZnCo_2O_4$ on Ti-mesh and a Ni plate serve as the working and counter electrodes, respectively. The sample is connected with a Ti wire and the Ni plate with Cu wire to the cables of the potentiostat. The setup itself is protected from air exposure with Teflon covered rubber and caps because dissolved CO_2 changes the pH value of the solution. In order to remove dissolved Oxygen and CO_2 from the solution, it is purged with Nitrogen for around 10–15 minutes. However, the cell cannot be completely sealed off from air, since needles are needed to let out the produced gases and holes for the reference electrode and wires (Fig. 4.8 b). The solution is stirred by a small ceramic "fish" with a magnetic material inside, placed on a magnetic stirrer. A rotation speed of around 300-350 rounds per minute (rpm) already ensures sufficient movement of the electrolyte to remove bubbles from the catalyst surface, providing "new" water molecules preventing deactivation of the WE and therefore, reducing mass-transfer limitations.

Two types of measurements are performed. During *cyclic voltammetry* (CV) the potentiostat linearly sweeps the voltage between two values for a given number of cycles and scan rate. Secondly, *chronoamperometry* probes the stability and performance of the catalyst by applying a constant voltage and recording the current–time dependence. The longer there is no change in current during opertion the more stable the system is. Naturally, many processes in the cell can affect its stability, for instance oxidation/corrosion of the wires leading to additional resistance, change of pH of the solution, contamination

of sample or substrate for example with carbon species, and accumulation of bubbles on the electrodes. Alternatively, the peak current value of many CV scans can also be studied over time. Since the voltage applied by the potentiostats can not be slowly ramped to the desired potential but is rather applied in an instant, the catalyst might be damaged due to capacitive effects when starting the chronoamperometry measurements.

4.3.2. Calibration of the Hg/HgO reference electrode

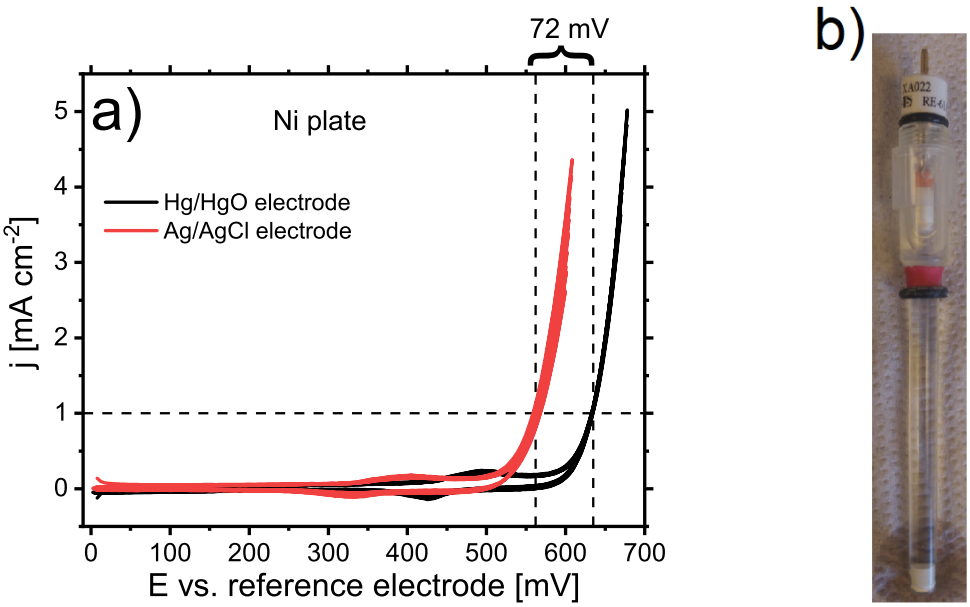

Figure 4.9.: Resulting CVs of the calibration measurement (a) and photograph of a Hg/HgO reference electrode (b).

Since 1M KOH is very alkaline, a suitable and stable reference electrode is required. Reported values of the standard potential $E^0_{\text{Hg/HgO}}$ of the RE range from 0.9258 V to 0.1 V [26, 29, 30]. An Ag/AgCl RE proved not to be suitable for a longer period of time, resulting in diffusion of chlorine into the cell causing potential shifts. Therefore, calibration cyclic voltammetry of 10 scans is performed with Ni plates as WE and CE, once with a 3M KCl Ag/AgCl reference electrode (with known $E^0_{\text{Ag/AgCl}} = 0.21\,\text{V}$ vs. SHE), and once with the 1M KOH Hg/HgO electrode. The potentials where $1\,{}^{\text{mA}}/_{\text{cm}^2}$ are achieved, are compared (Fig. 4.9 a). The current reaches $1\,{}^{\text{mA}}/_{\text{cm}^2}$ at mean values of 563 mV and 635 mV

vs. Ag/AgCl and Hg/HgO reference electrodes, respectively. Therefore, the difference is $E_{\mathrm{Hg/HgO}} - E_{\mathrm{Ag/AgCl}} = -72\,\mathrm{mV}$. That means $E^0_{\mathrm{Hg/HgO}} = 0.21\,\mathrm{V} - 0.072\,\mathrm{V} = 0.138\,\mathrm{V}$ vs. SHE. However, the result may be altered due to the lack of stability of the Ag/AgCl electrode and resulting potential shifts.

4.3.3. Photoelectrochemistry

In principle, a photoelectrochemical cell is built the same way as a conventional electrochemical cell. It consists of a working, a counter and a reference electrode (1M KOH Hg/HgO). In order to be able to harvest the light energy the catalyst is not dipped into solution but placed directly on the top side of a flow cell (Fig. 4.10 a). A *FYTRONICS FY 7000 Solar Simulator* illuminates the working electrode from above (cf. Fig. A.1 in the Appendix). It is possible to tune the intensity from 0 to 100 $^{\mathrm{mW}}/_{\mathrm{cm}^2}$ in steps of 20 $^{\mathrm{mW}}/_{\mathrm{cm}^2}$. Due to the rather low conductivity of $ZnCo_2O_4$ (sample size $7 \times 7\,\mathrm{mm}^2$) a transparent and conducting back electrode - 2% Al:ZnO ($10 \times 10\,\mathrm{mm}^2$) - is required. For contacting, a Cu wire is Indium-soldered to one edge of the sample. A small Pt plate is used as the CE.

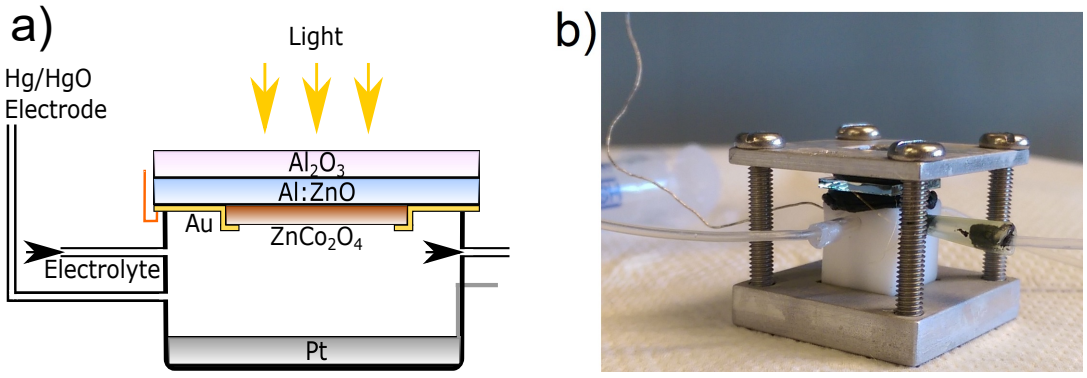

Figure 4.10.: Schematic view and photograph of the used flow cell with tubes.

The flow cell is built up of a Teflon cube (volume $\sim 1\,\mathrm{cm}^3$) screwed between an Al base and top plate with a hole of $1\,\mathrm{cm}^2$. On top of this cube the sample is placed up-side down between two seal rings (Fig. 4.10 b). Since generated Hydrogen and Oxygen bubbles will move up, potentially blocking the reaction or forming Oxyhydrogen, a continuous flow of

the 1M KOH electrolyte through the cell is applied by tubes. A container filled with it is placed higher than the collecting vessel after the cell. That way, a flow of $400 - 500\,{}^{\mathrm{ml}}/_{\mathrm{h}}$ is achieved, constantly carrying fresh water to the catalyst surface and removing the produced gases.
Although the cell design is very simple compared to improved, 3D-printed versions [54], it has to be mentioned that sealing the cell is not an easy task. The connection of the tubes to the cell or the seal rings and sample might be untight due to uneven screwing or tilting, resulting in air inside the cell and/or tubes. Even the tiniest hole is enough for the KOH to leak and to disturb or even stop the flow by sucking in air. Air bubbles in the tube to the reference electrode might block the electrical contact to the potentiostat. Additionally, if air accumulates beneath the catalyst, not only the activity could be reduced but the electrical connection to the electrolyte can be cut off completely, as well. Therefore, the holes for the tubes were sealed using cut pipette tips with the tubes tucked in and glued with bitumen and Parafilm films. The cap of the cell was sealed by putting some Silicon vacuum grease on the bottom side of the lower seal ring and carefully placing and screwing the sample and the top part to the base plate. Syringes were used to inject the electrolyte into the system and to create the initial pressure for its flow. The Pt wire of the CE is guided through another small hole on one side of the cell and connected to the potentiostat with a clamp. It is sealed with nail polish and glued to the base, reducing mechanical strain. The PEC cell is connected to the JAISSLE potentiostat and CV measurements are performed.

5
Experimental Results

In this chapter, the experimental results will be presented. They include crystallographic investigations by XRD of $ZnCo_2O_4$/Ti-mesh, $ZnCo_2O_4$/2%Al:ZnO/Al_2O_3 samples and reference films. Additionally, x-ray and Auger spectroscopy analysis due to possible changes of the catalyst surface during electrochemistry experiments has been done. Finally, the findings of electro- and photoelectrochemical experiments of the $ZnCo_2O_4$ in H- and flow cell are discussed separately. Both these discussions will be divided into measurements via cyclic voltammetry with overpotential, Tafel analysis and long-term performance tests by chronoamperometry.

5.1. X-Ray Diffraction

XRD measurements are performed to gain insight into the crystal structure, lattice parameters and possible Co:ZnO phases in the $ZnCo_2O_4$ spinel on different substrates. To be more specific, 200 nm $ZnCo_2O_4$ on Al_2O_3 and on a Ti-mesh are investigated for their use in conventional electrochemical experiments. As a reference, a 200 nm $ZnCo_2O_4$/300 nm Ti/Al_2O_3 sample was grown. The $ZnCo_2O_4$ is grown as explained in section 4.1. The titanium film is grown by PLD at room temperature with an O_2 : Ar ratio of $10 : 0$ sccm. Since a transparent electrode is required for photoelectrocatalysis, a 350 nm $ZnCo_2O_4$/300 nm 2%Al:ZnO on Al_2O_3 sample is studied. The samples on Al_2O_3 were studied using the hybrid beam optics, the ones on the mesh with the graded W/Si mirror (resulting in higher intensity but less resolution).

The result of a $2\theta - \omega$ scan of the $ZnCo_2O_4$/Al_2O_3 reference sample shows a sharp and intense Al_2O_3(006) substrate peak at $2\theta = 41.6822\,^\circ$ and several peaks which are

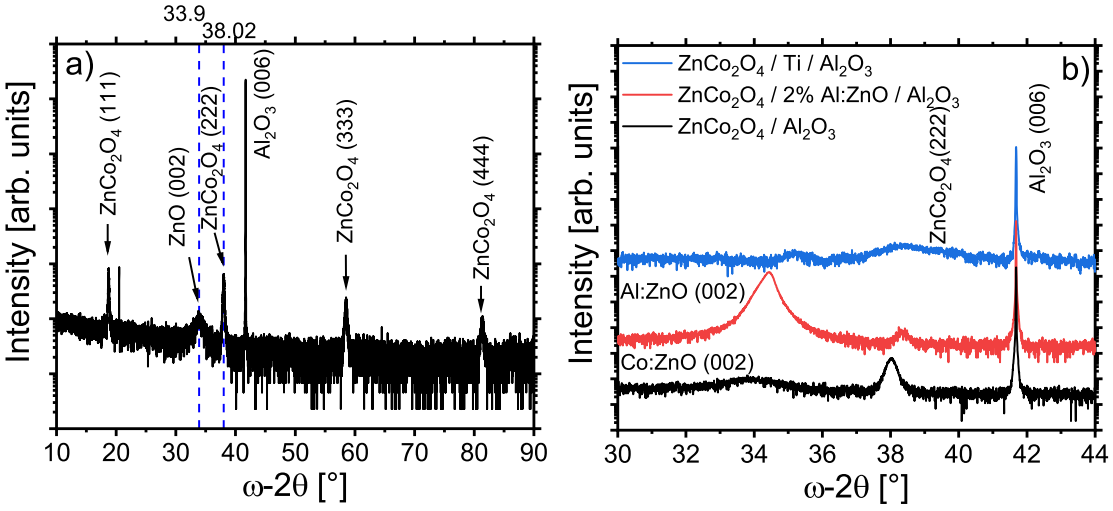

Figure 5.1.: XRD measurements of $ZnCo_2O_4/Al_2O_3$ (a), and comparison with intermediate Ti or AZO films (b).

identified as multiples of the $ZnCo_2O_4$ (111) reflection (Fig. 5.1 a). Due to the step size of the diffractometer ($0.005\,°$) and Voigt-fit errors of OriginLab, the error is estimated to be in the order of approximately $\frac{1}{100}\,°$. Therefore, the $ZnCo_2O_4$ (222) reflection is located at $2\theta = (38.02 \pm 0.01)\,°$ with a FWHM of $0.28\,°$. However, a (Co:)ZnO (002) peak is present at $2\theta = (33.90 \pm 0.01)\,°$ (FWHM $= 1.56\,°$), as well. The ZnO reflection indicates wurtzite phases in the $ZnCo_2O_4$, although the intensity of that peak is smaller by almost an order of magnitude and the FWHM over five times larger. Moreover, in contrast to previous research [41], no higher orders are observable. Therefore, the $ZnCo_2O_4$ mainly grows well in the cubic spinel crystal structure, with some wurtzite secondary phases. Using the (222) Bragg peak, the lattice parameter along the growth direction is calculated by equ. 2.32 to $c = (8.192 \pm 0.002)\,\text{Å}$, close to reported values of $8.08\,\text{Å}$ [46]. The deviation might be explained by the columnar growth of the Zinc oxides by reactive magnetron sputtering and the presence of the wurtzite ZnO phase in the $ZnCo_2O_4$, causing distortion in the lattice.

If $ZnCo_2O_4$ is grown onto intermediate layers, for instance Ti or AZO, shifts in both the ZnO (002) and $ZnCo_2O_4$ (222) reflections are observed (Fig. 5.1 b). The Al:ZnO peak shifts to $2\theta = (34.41 \pm 0.01)\,°$ (FWHM $= 0.35\,°$), corresponding to an out-of-plane lattice constant $c = (5.208 \pm 0.001)\,\text{Å}$ in very good agreement with $5.213\,\text{Å}$ in Ref. [37]. The $ZnCo_2O_4$ (222) peak at $2\theta = (38.33 \pm 0.01)\,°$ (FWHM $= 0.36\,°$) is less intense, suggesting that the Al:ZnO grows with excellent quality on Al_2O_3. The lattice parameter of $ZnCo_2O_4$ is calculated to $c = (8.128 \pm 0.002)\,\text{Å}$. This value is closer to the reported

value of $8.08\,\text{Å}$ [46], which indicates that the $ZnCo_2O_4$ is growing in better crystal quality and less strained on AZO than on Al_2O_3. Unfortunately, since AZO is wurtzite type, no conclusive arguments can be made regarding the phase purity of $ZnCo_2O_4$, even if AZO/Al_2O_3 samples would have been grown for comparison. The more intense Al:ZnO peak would always dominate smaller Co:ZnO wurtzite peaks. However, from an optical point of view, grown samples still appear to be dark brown (cf. Fig. 4.3 c).

XRD of $ZnCo_2O_4$ with a 300 nm thick Ti layer on c-sapphire exhibits a broad and weak $ZnCo_2O_4$ peak at $2\theta = (38.53 \pm 0.01)\,^\circ$ (FWHM $= 1.93\,^\circ$) and probably Ti (100) at $2\theta = (35.19 \pm 0.01)\,^\circ$ (FWHM $= 0.66\,^\circ$) (Fig. 5.1 b). The lattice parameter of $ZnCo_2O_4$ is $c = (8.087 \pm 0.002)\,\text{Å}$ and fits perfectly to the reported value of $8.08\,\text{Å}$. It has to be mentioned that, theoretically, there are two more Titanium Bragg reflections in the vicinity [55]: Ti (002) and Ti (101) at $2\theta = 38.67\,^\circ$ and $2\theta = 40.44\,^\circ$, respectively. It is well possible that there is a peak overlap of the two materials due to the rather high full-width at half maximum. However, since no other Ti reflections are observed, it is assumed that the peaks are produced by the $ZnCo_2O_4$ on a nearly amorphous Ti intermediate layer. This is supported by the fact that growth of Ti at room temperature has not yet been optimized. Although the lattice parameter matches well with the theoretical value, the weak and broadened peak suggests that there is a big distribution of $ZnCo_2O_4$ lattice constants and the overall crystal quality of the spinel on Ti is poor.

Performing x-ray diffraction on a Ti-mesh turns out to be difficult, since there is no intense substrate peak for sample alignment procedures. Additionally, the mesh geometry itself complicates this process even further (uneven surfaces, possible bending of the mesh) so that no precise alignment was possible. Since little intensity was expected, the W/Si mirror beam optics was used[1], giving less resolution (other K_α lines are not blocked), but higher intensity.

Fig. 5.2 a) shows the symmetrical $2\theta - \omega$ scans of a Ti reference mesh and 200 nm $ZnCo_2O_4$/Ti-mesh. The vertical axis is not scaled logarithmically, but linearly. The characteristic hump of the glass slide in the XRD signal required background subtraction of the data. All titanium reflections are found at slightly lower angles (about $0.3\,^\circ$) compared to calculated values, probably due to poor alignment, but generally in good agreement with calculated values from materialsproject.com [55].

[1] The measurement with the hybrid optics resulted in a very noisy spectrum with less than 100 counts per second. No peaks were observable without smoothing the data.

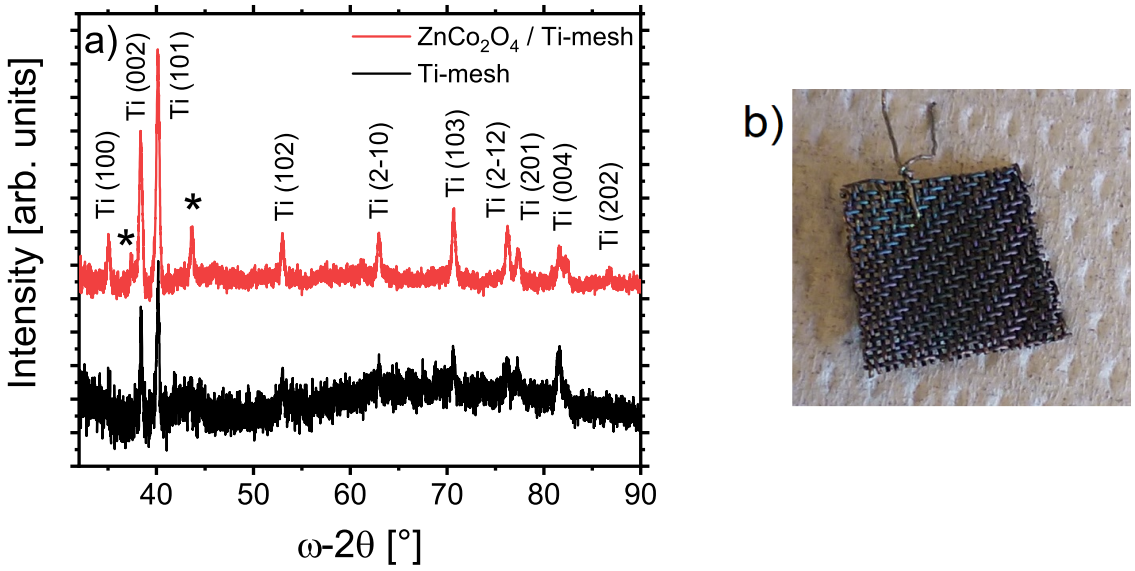

Figure 5.2.: $2\theta - \omega$ scans of Ti-mesh and $ZnCo_2O_4$/Ti-mesh (a), and picture of a $ZnCo_2O_4$ sample (b)

Titanium(di-)oxide reflections can be excluded [56, 57], since no such peaks are visible. Ti is known for its passivating ability due to the formation of a thin, protecting natural oxide layer [58]. This barrier protects the metal from surrounding media. It is built immediately after contact with air at atmospheric pressure and is very stable. The initial oxide layer thickness is around $12-16\,\text{Å}$ and reaches only $50\,\text{Å}$ after 70 days. Afterwards, diffusion processes still happen, but very slowly ($250\,\text{Å}$ after 4 years). The passivating oxide layer is expected to be amorphous rather than having any specific crystal structure. Since this layer is very thin compared to the Ti beneath, the XRD signal would be very weak and therefore barely detectable.

Apart from the found Ti peaks, two new Bragg reflections arise (marked with asterisks "*"), a small one at $2\theta = 37.42\,°$ (FWHM $= 0.49\,°$) and one at $2\theta = 43.65\,°$ (FWHM $= 0.34\,°$). The first one might be interpreted as a $ZnCo_2O_4$ (222) peak. Deviations from the peak positions on planar substrates (Fig. 5.1) are very likely, as the substrate is not planar and no epitaxial film on an uneven mesh structure is expected. Concerning the second peak, the theoretical value for a CoO (002) peak is at higher angles of $2\theta = 44.34\,°$ [59] and thus, it can not be clearly allocated. In conclusion, it can be said that on the one hand, the $ZnCo_2O_4$ film is assumed to be more amorphous than a cubic spinel crystal because of the geometry of the mesh with uneven surfaces on its strings (Fig. 5.2 b). On the other hand, $ZnCo_2O_4$ grows well on Al_2O_3 substrates and 2%Al:ZnO.

5.2. X-Ray Photoelectron Spectroscopy

In order to investigate the chemical state of the samples, XPS measurements were conducted. The main goal of this analysis is to examine the oxide nature of the samples on the surface. As sample systems serve a Ti film, grown on sapphire and a Ti-mesh. After XPS measurements of the substrates, a 200 nm $ZnCo_2O_4$ film was grown on top and the sample transferred back to the XPS chamber without breaking the vacuum, preventing surface contamination with air and carbon. The main XPS regions for cobalt, zinc and titanium are the 2p states, with L_2 and L_2 denoting the $2p_{1/2}$ and $2p_{3/2}$ states, respectively.

The theoretical peak positions of metallic Zn and Co are: Zn L_3 and L_2 with $E_B = -1021.8\,\mathrm{eV}$ and $E_B = -1044.9\,\mathrm{eV}$, respectively, and Co L_3 and L_2 with $E_B = -778.1\,\mathrm{eV}$ and $E_B = -793.2\,\mathrm{eV}$, respectively [60]. If the cobalt atoms in the solid are bound, e.g., to oxygen, the binding energy changes due to the chemical shift, and additional sattelites appear, with splitting of $9.3\,\mathrm{eV}$ and $9.4\,\mathrm{eV}$ for the Co L_3 and L_2 satellite peaks, respectively [61, 62]. The chemical shift of ZnO is not as pronounced, with its L_3 peak position only changing by a few tenth of eV [62]. Thus, in contrast to metallic cobalt samples with two 2p peaks, four characteristic peaks can be found in Co–O films and the chemical nature of the $ZnCo_2O_4$ samples can be investigated. The L_3 and L_2 states of Ti correspond to binding energies of $E_B = -453.8\,\mathrm{eV}$ and $E_B = -460.2\,\mathrm{eV}$ [60].

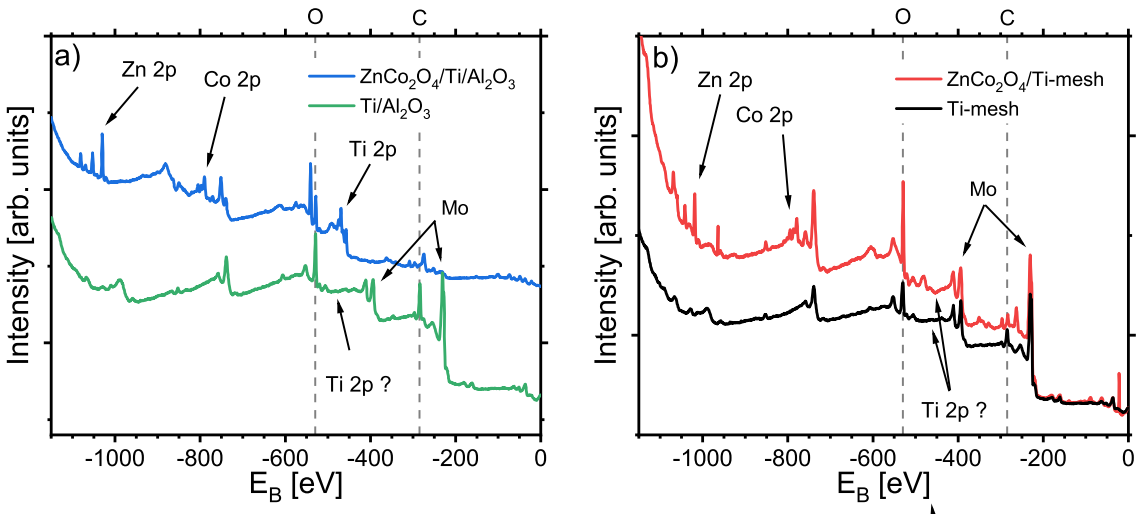

Figure 5.3.: XPS scans of reference films with Ti and $ZnCo_2O_4$/Ti on sapphire (a) and $ZnCo_2O_4$ on Ti-mesh (b).

The resulting XPS spectra are shown in Fig. 5.3. On the $300\,\mathrm{nm}$ Ti-film/Al_2O_3 reference sample (without $ZnCo_2O_4$), neither Co nor Zn peaks arise. Interestingly, during this measurment, no Ti peaks its main XPS region (L_2 and L_3 states) - according to [60] - were found either (Fig.5.3 a). In contrast to that, molybdenum (Mo) from the back plate was detected. When $200\,\mathrm{nm}$ $ZnCo_2O_4$ are grown ontop, Zn and Co are clearly visible (Fig. 5.3 a). Zn L_2 and L_3 peaks are found at $-1054\,\mathrm{eV}$ and $-1031\,\mathrm{eV}$, whereas Co L_2 and L_3 possess binding energies of $-798\,\mathrm{eV}$ and $-781\,\mathrm{eV}$ with satellite splittings of around $7\,\mathrm{eV}$ and $8\,\mathrm{eV}$, respectively. The measured peak positions are shifted by several eV, indicating Zn-O and Co-O species on the surface of the film. Two satellites for the Co-O peaks are detected, as well. Surprisingly, on the final $ZnCo_2O_4$/Ti film, titanium 2p peaks are present in the spectrum with a L_3 peak position of $E_B = -458\,\mathrm{eV}$, meaning that titaniumoxide is present in the sample [60, 62].

Regarding the samples on the mesh, on both specimen (a plain Ti-mesh and the same mesh coated with $ZnCo_2O_4$), Ti peaks are *not* visible in the XPS spectra, even after re-aligning several times (Fig. 5.3 b). However, due to the mesh geometry of the sample, revealing the molybdenum back plate, Mo 3d and 3p peaks are visible.

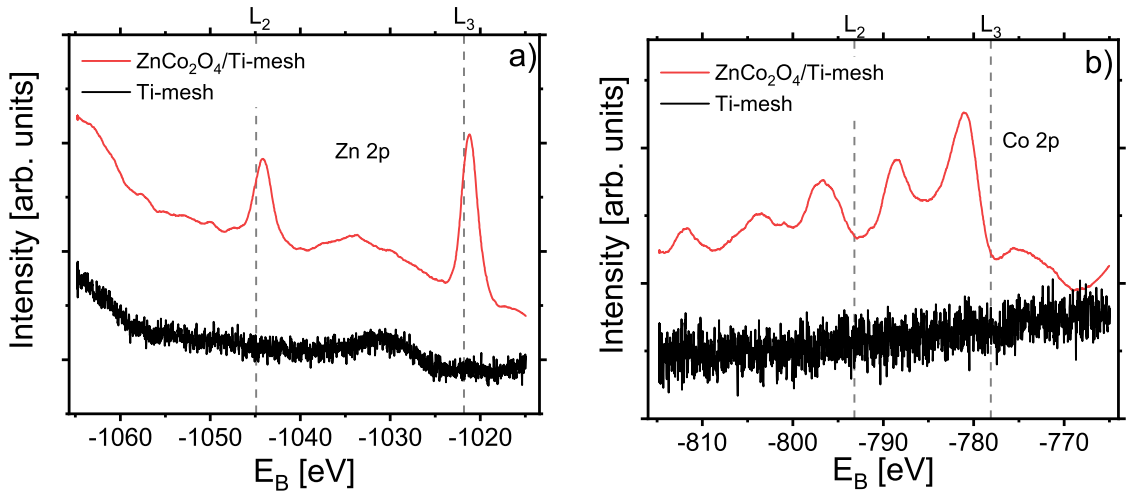

Figure 5.4.: Zn (a) and Co (b) XPS spectra of a $ZnCo_2O_4$/ Ti-mesh sample compared to a plain mesh with higher resolution.

A closer look at the zinc and cobalt regions on the mesh with higher resolution can be seen in Fig. 5.4. The Zn 2p states are detected at binding energies of $-1044\,\mathrm{eV}$ and $-1021\,\mathrm{eV}$. The L_3 and L_2 peaks of cobalt, shifted to higher binding energies with

respect to the metallic Co position, are found at $E_B = -781\,\mathrm{eV}$ and $E_B = -796\,\mathrm{eV}$, respectively. Corresponding satellites with splitting of around $7\,\mathrm{eV}$ and $8\,\mathrm{eV}$ are observed, well demonstrating the Co–O nature of the $ZnCo_2O_4$ on the mesh [60, 62].
However, the exact peak positions have to be treated with caution. The aperature is quite old and the electronics of the analyzer rather unstable. Therefore, precise measurements are not possible and combined with potential corrosion of the contacts, absolute binding energies are fraught with errors estimated to be in the order of at least several hundred meV. This is evident by, for example, looking at the peaks from bound oxygen and carbon atoms in Fig. 5.3. Their positions are slightly different for every measurement (around $-530\,\mathrm{eV}$ for O and $-285\,\mathrm{eV}$ for C). The presence of the C peak indicates some contamination of the samples.
To summarize the XPS results, in the grown $ZnCo_2O_4$ samples, the Zn and Co are not metallic but rather bound to O atoms, as evident by peak position shifts and satellite peaks. Although the absolute binding energies are not very meaningful due to the old electronics, the Co 2p satellites and their splitting (7 and 8 eV) match well with previous research (around 9 eV) [61]. The findings show that even if the crystal structure on the Ti-mesh is not perfect, the films do not exhibit metallic Co or Zn but their oxidized species, as expected for $ZnCo_2O_4$.

5.3. Electrocatalytic Properties of $ZnCo_2O_4$

The electrocatalysis of $ZnCo_2O_4$ is studied in an H-cell with Ni as counter electrode. The setup was placed on a magnetic stirrer (rotation speed $\approx 300 - 350\,\mathrm{rpm}$). All measurements were done in 1 molar potassium(bi-)carbonate and potassium hydroxide. Usually, at first cyclic voltammetry is done, by repeatedly sweeping the potential linearly (Linear sweep voltammetry). With the data from the obtained CVs, the overpotential and the Tafel slope are determined. Then, stability tests under continuous operation at a constant potential are done.

5.3.1. Cyclic Voltammetry

In Fig. 5.5 the CV measurements of 50 cycles for $ZnCo_2O_4$ on a Ti-mesh and a plain Ti-mesh in 1M $KHCO_3$ and K_2CO_3 are shown. The scan rate of the applied potential is 100 $^{\mathrm{mV}}/_{\mathrm{s}}$ and the used reference electrode is a 3M KCl Ag/AgCl reference electrode. The x-axis depicts the potential converted to RHE (cf. equ. 2.24). On the top, the overpotential $\eta = E - E^0_{H_2O} = E - 1.23\,\mathrm{V}$ is shown. The y-axis is the to the area normalized, produced current through the circuit (mesh surface area $\approx 0.83\,\mathrm{cm}^2$). The black arrows indicate the scan direction of the potential.

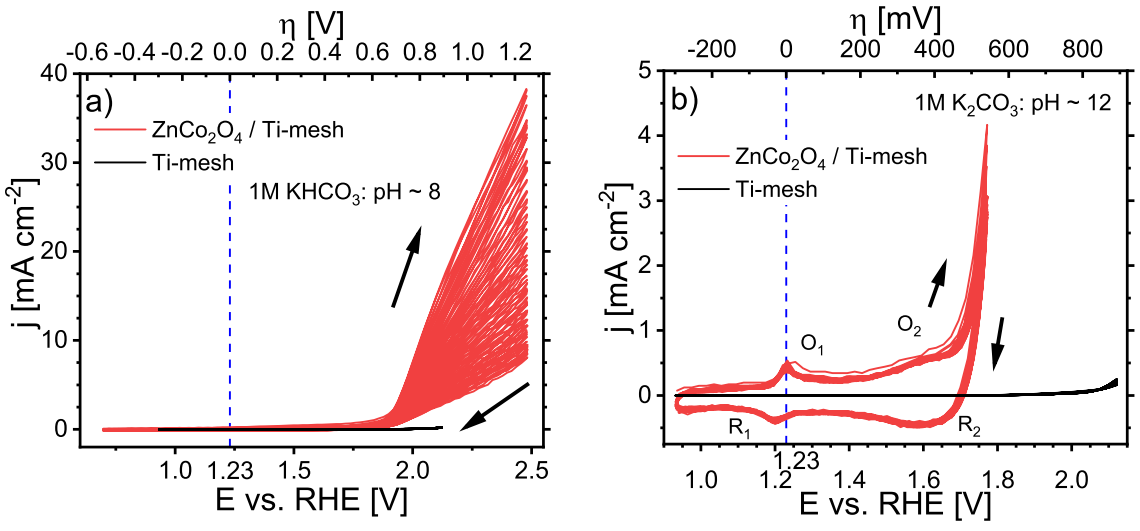

Figure 5.5.: Cyclic voltammetry of $ZnCo_2O_4$ on Ti-mesh in 1 molar potassium bicarbonate (a) and carbonate (b).

The current through the circuit in slightly alkaline 1 molar $KHCO_3$ (Fig.5.5 a), i.e. the reaction rate, significantly rises at around 1.9 V vs. RHE. The overpotential η (additional voltage to standard potential $E^0_{O_2}$) to drive the reaction is $810\ \mathrm{mV}$ at $10\ {}^{\mathrm{mA}}/_{\mathrm{cm}^2}$. The standard potential of 1.23 V is indicated by the blue, dahsed line. The plain Ti-mesh shows no sign of any catalytical effect up to around 2.2 V vs. RHE because the current stays below $0.25\ {}^{\mathrm{mA}}/_{\mathrm{cm}^2}$ in the scanned potential range. This result already demonstrates that $ZnCo_2O_4$ acts as a good electrocatalyst for the oxygen evolution reaction. Moreover, the Ti-mesh is a suitable substrate material, since it is both conducting ($\rho_e \approx 55 \cdot 10^{-6}\,\Omega\,\mathrm{cm}$ [63]) and inactive towards the OER [12]. However, it is apparent that with every cycle the activity of the catalyst reduces, resulting in lower currents cycle by cycle, indicating some stability issues. One explanation could be impurities on the catalyst or on the substrate which degrade the electrode under these rather hard working conditions, as the current in the plain Ti-mesh measurements also slowly drops with time (not clearly visible because of the scales in the graphs).

CVs in more alkaline solution (1M K_2CO_3 aqueous solution, pH ~ 12), once again, nicely demonstrate the catalytic activity of $ZnCo_2O_4$ compared to a plain Ti-mesh substrate. This system performs significantly better than in $KHCO_3$, since the current begins to increase a sooner at around 1.7 V vs. RHE. An overpotential at $10\,{}^{\mathrm{mA}}/_{\mathrm{cm}^2}$ cannot be determined because the current does not reach this point in the measured potential range, but is estimated to be at around $\eta \approx 550 - 600\,\mathrm{mV}$. Nevertheless, this system appears to be more stable towards the OER because over the measured 50 cycles, the reaction rate decreases much more slowly.

Intermediate oxidation/reduction peaks are observed in both of the measurements, but are better visible in Fig. 5.5 b), because these redox peaks are just the size of a fraction of 1 ${}^{\mathrm{mA}}/_{\mathrm{cm}^2}$ and therefore not visible in Fig.5.5 a). The peak positions O_1/R_1 and O_2/R_2 are at around $1.2\,\mathrm{V}$ and $1.6\,\mathrm{V}$ vs. RHE. Previous research found that they are very sensitive to the surface morphology and composition of the catalyst, may also be a contribution of the substrate and the peak sizes vary from study to study [13]. Kim et al. [11] even report the absence of such peaks. If the observed peaks arise from $ZnCo_2O_4$, the O_1/R_1 and O_2/R_2 correspond to the O^{2+}/O^{3+} and O^{3+}/O^{4+} redox couples, according to Ref. [13].

In Fig 5.5 b), hysteresis-like opening of the CV can be observed, as well. The forward scan and the backward scans are not the same. This is an artefact of the scan rate, how

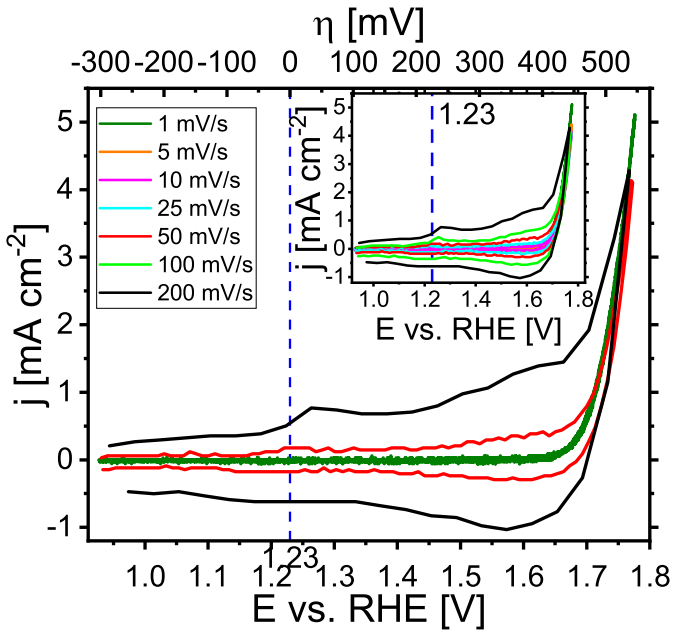

Figure 5.6.: CVs of $ZnCo_2O_4$ with different scan rates from $1 - 200\,^{\mathrm{mV}}/_{\mathrm{s}}$ in 1M K_2CO_3.

fast the potential is sweeped over time. In order to demonstrate that, cyclic voltammetry measurements of the $ZnCo_2O_4$ / mesh samples were done with scan rates ranging from $1 - 200\,^{\mathrm{mV}}/_{\mathrm{s}}$. Below scan rates of around $10\,^{\mathrm{mV}}/_{\mathrm{s}}$ the hysteresis closes and the redox peaks disappear, as a "steady-state" is approached (Fig. 5.6). For better visibility, only the measurements with scan rates of $200\,^{\mathrm{mV}}/_{\mathrm{s}}$, $50\,^{\mathrm{mV}}/_{\mathrm{s}}$ and $1\,^{\mathrm{mV}}/_{\mathrm{s}}$ are shown enlarged. All other scan rate measurements are shown in the inset of the graph. At higher scan rates the redox peaks are still present, whereas for low scan rates, no hysteresis or peaks are recognizable and the forward and backward scans are identical.

Changing from Ag/AgCl to a more stable 1M KOH Hg/HgO reference electrode and a higher purity Ti-mesh from another manufacturer (Good fellow [64]) makes the catalyst more effective and stable, even in highly alkaline 1 molar potassium hydroxide with pH values of appoximately 13.8-14 (Fig. 5.7). The water splitting process is even further enhanced, compared to potassium carbonate and bicarbonate. The reaction rate rapidly increases already at around $1.6\,\mathrm{V}$ vs. RHE, exhibiting an astonishing overpotential of only $\eta = 390\,\mathrm{mV}$ at $10\,^{\mathrm{mA}}/_{\mathrm{cm}^2}$, coming very close to reported promising earth-abundant metal oxide catalysts like $NiFeO_x$ ($\eta = 350\,\mathrm{mV}$) or $NiCoO_x$ ($\eta = 380\,\mathrm{mV}$) [9]. The first cycle - often called "virgin curve" is usually a bit different from the rest of the scans, as apparent in Fig. 5.7 a,b).

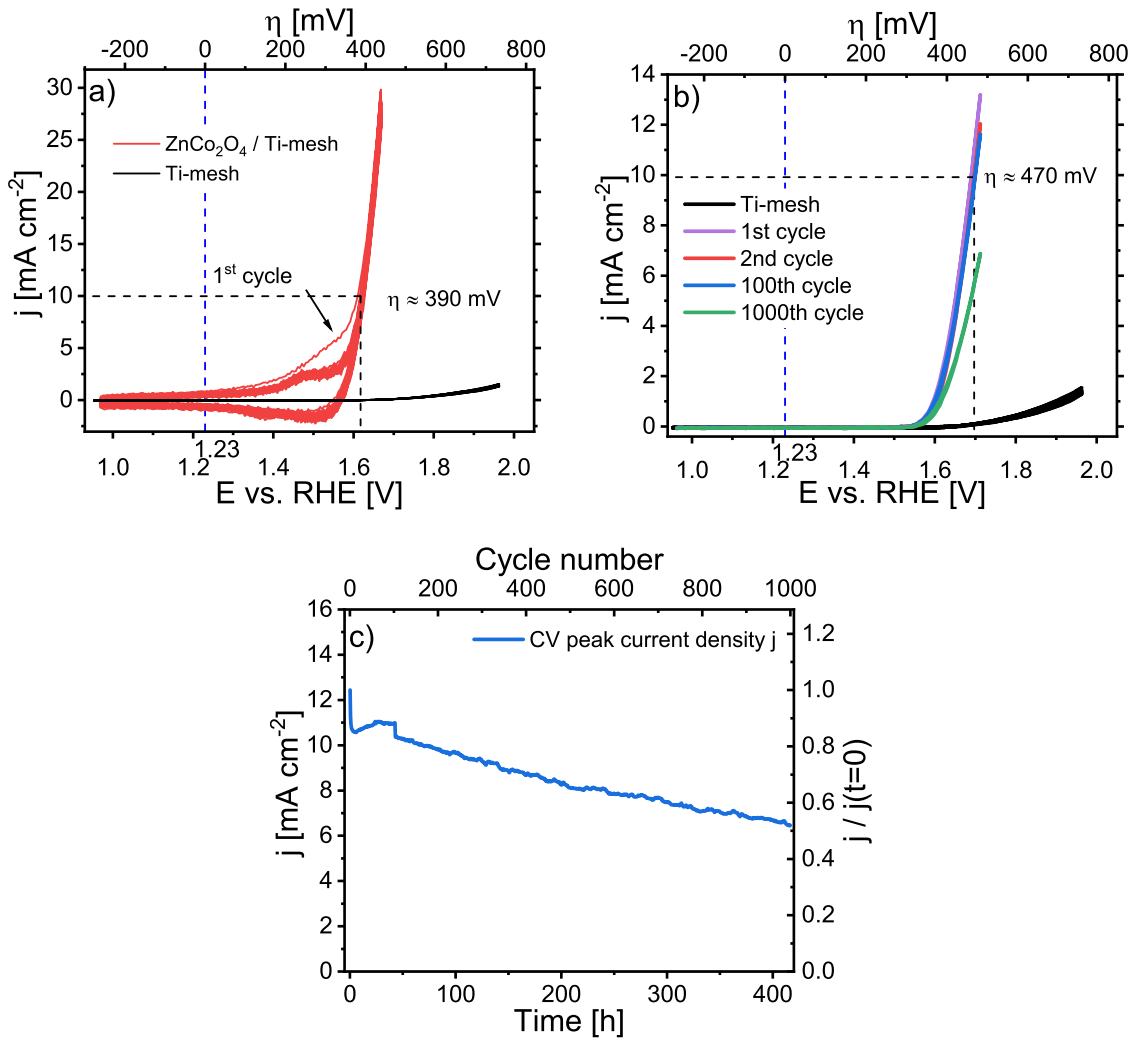

Figure 5.7.: Cyclic voltammetry measurements of $ZnCo_2O_4$ on a high-purity mesh from Good Fellow with a 1M KOH Hg/HgO reference electrode (a,b) and peak current density values of (b) for over 400 hours (c).

Over the 50 measured cycles of the measurement in Fig. 5.7 a), there is no significant drop in current, suggesting a very stable system. A redox peak pair is visible at around $1.5\,\mathrm{V}$ vs. RHE, as well, because this measurement was done with a faster scan rate of $50\,{}^{\mathrm{mV}}/_{\mathrm{s}}$. Fig. 5.7 b) shows the first, the second, the hundredth and the one thousandth cycle of CV measurements for another $ZnCo_2O_4$ sample over 1000 cycles (scan rate $1\,{}^{\mathrm{mV}}/_{\mathrm{s}}$), demonstrating the ability of the system to operate for 1000 cycles. In this case, the overpotential of $470\,\mathrm{mV}$ at $10\,{}^{\mathrm{mA}}/_{\mathrm{cm}^2}$ is higher. The peak values of every cycle is shown in Fig. 5.7 c). After 1000 cycles (corresponding to around 416 hours),

the peak current value is still 52% of its initial value. However, it is clearly evident that measurement conditions are of huge importance, since slight changes in surface morphology and catalyst working conditions can have big effects. But they are quite difficult to maintain: the Ti mesh has to be clean and free of oxygen on the surface, the molar concentration of the KOH should always be exactly 1 molar, the contacts from the sample to the potentiostat should be perfect, corrosion avoided and the sample surface morphology must be the same for every measurement.
After repeating the measurements several times, overpotentials in the range of $\eta \approx 390 - 470\,\mathrm{mV}$ at $10\,{}^{\mathrm{mA}}/_{\mathrm{cm}^2}$ are obtained. The uncertainty in η might be caused by the above mentioned difficulty of creating the exact measurement conditions for every experiment. Another reason might be that the CVs in Fig. 5.7 a) were done shortly after receiving a new Ti-mesh from Good fellow, which might have still been very clean, resulting in lower overpotentials. After doing experiments several weeks later, the exposure to air could have contaminated the surface of the mesh with oxygen (a passivating layer of TiO_x), causing additional resistances within the system even after cleaining procedures with high purity water and isopropanol. This resistance, combined with the experimental conditions, seemingly are enough to shift the reaction to higher potentials. However, the $ZnCo_2O_4$ /Ti-mesh catalyst proves to be highly catalytic towards the oxygen evolution reaction and is stable for 1000 cycles of operation ($>$ 416 hours) with overpotentials close to efficient transition metal catalysts [9]. A further measure of efficiency is the Tafel slope which will be analyzed in the following paragraphs.

5.3.2. Tafel Analysis

Tafel plots are made by plotting the measured CV curves $\eta = E - E^0$ vs. j logarithmically (see section 2.4). In this thesis, always the forward scan of second cycle (after the "virgin curve") is considered. This cycle best represents the measured data because it is the first after the virgin cycle and the impact of possible stability issues and degradation is still minimal. The non-linear parts and $\eta < 0$ are neglected because negative overpotential does not have any physical meaning in the case of the oxygen evolution reaction. The Tafel slope is then determined by a linear fit, as exemplarily shown in Fig. 5.8 for a Ni plate in 1 molar KOH.

The y-axis depicts the overpotential $\eta = E - 1.23\,\mathrm{V}$ and the x-axis the produced current

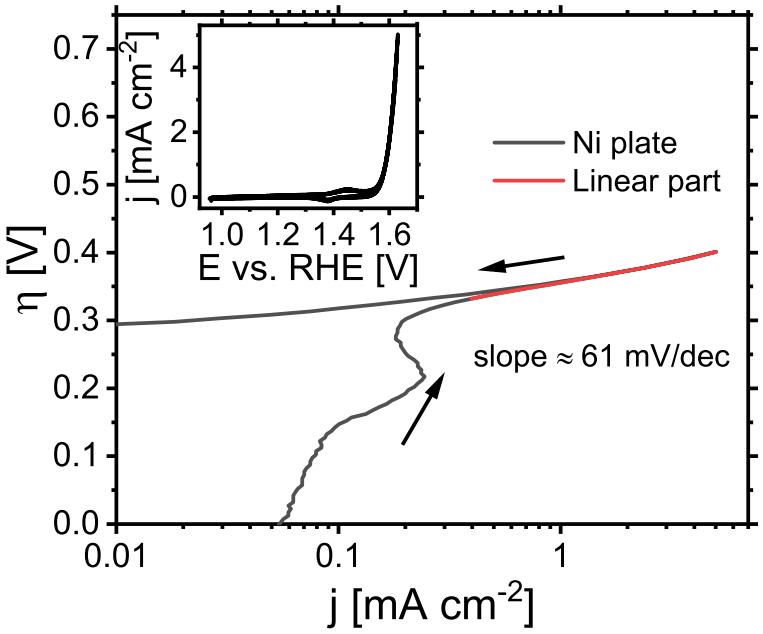

Figure 5.8.: Tafel plot of a Ni plate in 1 molar KOH with corresponding 20 cyclic voltammetry scans.

density j on a logarithmic scale. The inset of the graph shows the cyclic voltammetry measurements of the used Ni plate. The linear part of the (second) forward scan taken for fitting is marked in red, the black arrows indicate the scan direction of the potential. Before the linear part, a small oxidation peak of the Ni can be seen, as well (at an overpotential of around $\eta \approx 0.2\,\mathrm{V}$). A Tafel slope of around $61\,{}^{\mathrm{mV}}/_{\mathrm{dec}}$ is determined. Concerning efficiency, the lower the slope, the better the kinetics of the OER and less potential is required to increase the current by one magnitude. In the case of the Ni plate, $61\,\mathrm{mV}$ are required to increase the current density, i.e. the reaction rate, by one order of magnitude.

Concerning $ZnCo_2O_4$ catalysts, Fig. 5.9 shows that high alkaline solutions (KOH) make the OER catalysts more efficient than, e.g., 1M K_2CO_3, because they exhibit lower overpotentials η at higher current densities. For example, $ZnCo_2O_4$ samples measured in potassium carbonate show an overpotential of $\eta \approx 470\,\mathrm{mV}$ at $1\,{}^{\mathrm{mA}}/_{\mathrm{cm}^2}$, whereas the Ni plate in KOH only requires $360\,\mathrm{mV}$. The grey, dashed vertical lines illustrate the measured current density values of 1 and $10\,{}^{\mathrm{mA}}/_{\mathrm{cm}^2}$. The two $ZnCo_2O_4$ samples on Ti-mesh exhibit different overpotentials and linear parts at different current density values. The Tafel slopes are $103\,{}^{\mathrm{mV}}/_{\mathrm{dec}}$ (blue line, starred) - corresponding to Fig. 5.7 a) - at $10\,{}^{\mathrm{mA}}/_{\mathrm{cm2}}$ and $56\,{}^{\mathrm{mV}}/_{\mathrm{dec}}$ at around $1\,{}^{\mathrm{mA}}/_{\mathrm{cm}^2}$ (green line) - corresponding to Fig. 5.7

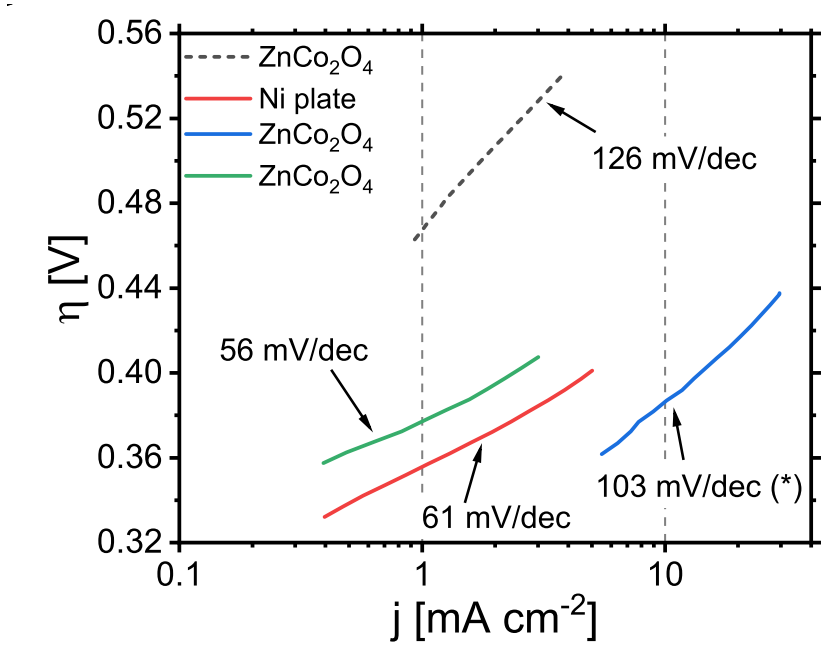

Figure 5.9.: Tafel plot of $ZnCo_2O_4$/ Ti-mesh samples and a Ni plate as reference in 1 molar potassium hydroxide potassium carbonate (dashed).

b) - with overpotentials of $470\,\mathrm{mV}$ and $390\,\mathrm{mV}$ at $10\,{}^{\mathrm{mA}}/_{\mathrm{cm}^2}$. At low current densities $ZnCo_2O_4$ seems to be very efficient in terms of Tafel slopes comparable to Kim et al. [11] who report Tafel slopes of $46\,{}^{\mathrm{mV}}/_{\mathrm{dec}}$ at current densities j around $1\,{}^{\mathrm{mA}}/_{\mathrm{cm}^2}$ which increase to higher values at higher reaction rates, estimated to be around $80-100\,{}^{\mathrm{mV}}/_{\mathrm{dec}}$. The obtained Tafel slopes indicate that the last step in the OER is the rate-determining step [27]: $OOH^* + OH^- \longrightarrow * + O_2 + H_2O + e^-$ (equ. 2.10), because Tafel slopes of around $30 - 40\,{}^{\mathrm{mV}}/_{\mathrm{dec}}$, and $120\,{}^{\mathrm{mV}}/_{\mathrm{dec}}$ at higher overpotentials have been calculated, which is in good agreement with the measured values. If equ. 2.10 is the rate-determining step, that means that the formation of O_2 from the surface adsorbed OOH and OH^- is the limiting reaction of the OER of $ZnCo_2O_4$ on Ti-meshes, probably caused by too high binding energies of oxygen to the surface atoms.

In summary, $ZnCo_2O_4$ on Ti-mesh is a highly catalytical and efficient catalyst for facilitating the oxygen evolution reaction. The best results are obtained in 1M KOH aqueous solution with low overpotentials close to promising earth-abundant metal oxide catalysts like $NiFeO_x$ ($\eta = 350\,\mathrm{mV}$) or $NiCoO_x$ ($\eta = 380\,\mathrm{mV}$) [9], and Tafel slopes also comparable to reported values [11].

5.3.3. Chronoamperometry & Auger Electron Spectroscopy

Finally, the stability of the catalytic system is tested by chronoamperometry. During that measurement, a constant voltage is applied and the current recorded vs. time. Since the catalyst showed strong degredation in bicarbonate during CV measurements but proved to be more stable in carbonate, a long-term stability test in 1M K_2CO_3 aqueous solution was performed. A voltage corresponding to an overpotential of 490 mV is applied and the resulting current is recorded for over 150 hours (Fig. 5.10).

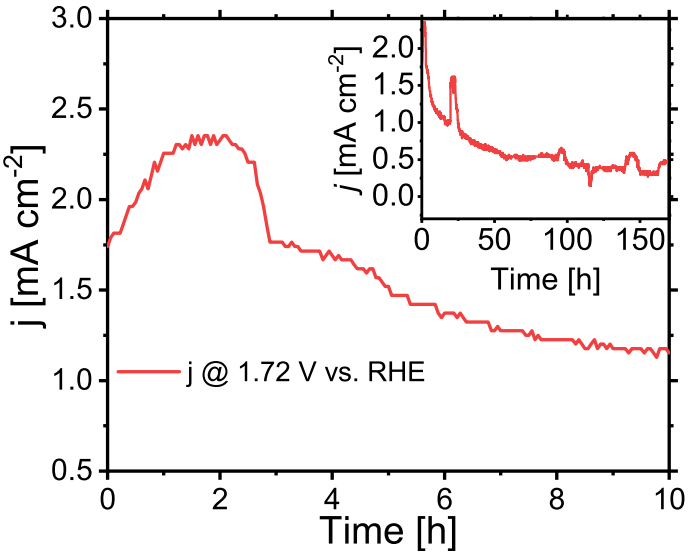

Figure 5.10.: Chronoamperometry measurement of $ZnCo_2O_4$ in 1M K_2CO_3.

In the first 3 hours, a rise in current is observed which then begins to drop. Throughout the 150 hours, several spikes and sudden drops in current are measured, which are indications for the dissolution of the catalyst and/or the substrate. Instabilites can arise from various processes. For efficient oxygen evolution, alkaline solutions and high oxidizing potentials have to be employed. Thus, the catalyst is operating under high strain. A combination of these extreme conditions and impurities on the anode can result in the dissolution of the catalyst because of the rise in local current density [28, 65].

Before and after the chronoamperometry measurements, Auger electron spectroscopy was performed[2], revealing that the surface of the mesh is covered with a big amount of

[2]The measurements were carried out by Dr. Jiri Duchoslav of ZONA institute.

carbon (90 at%), but also traces of chlorine and sulfur were found, which are generally catalyst poison, causing deactivation in various catalytic processes [66, 67].

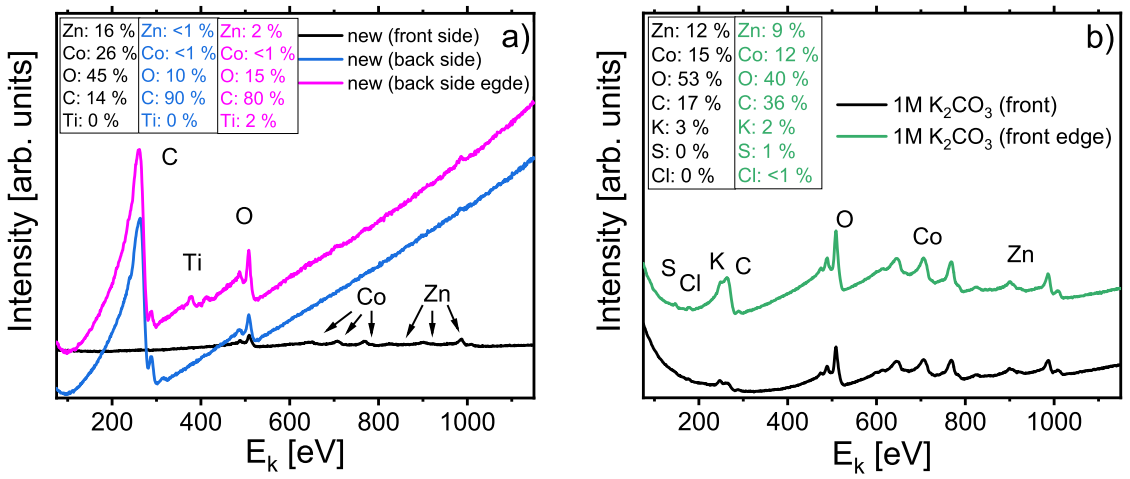

Figure 5.11.: Auger electron spectroscopy measurements with a new $ZnCo_2O_4$ sample (a) and after long-term stability tests in 1 molar K_2CO_3 (b).

Apparently, the initially bought Ti-mesh is contaminated by big amounts of carbon - even after cleaning processes with isopropanol and water in ultrasonic bath for 15-20 minutes. Fig. 5.11 a) displays the AES measurements of a fresh $ZnCo_2O_4$ /Ti-mesh sample of the front (in the middle and at the egde of a string) and the back side. The mesh is fully covered, not only in the middle, with the metal oxide because Zn, Co and O peaks in their right stochiometry were found ($Zn : Co : O \approx 1 : 2 : 4$), but no Ti peaks. Carbon species were detected as well (14 at%), probably resulting from the exposure to air and carbondioxide. However, the back side of the mesh was found to be very dirty, covered with at least 80 at% of carbon compounds, completely shielding off the Ti from the mesh itself due to the thickness of the layer.

During chronoamperometry, cobalt seems to be lost from the catalyst, as the element's content is reduced from 25% to 12-15% (Fig. 5.11 b). No significant changes are observed in the Zn content on the surface. However, potassium, sulfur and chlorine are detected as well, after electrolysis. K obviously stems from the potassium carbonate solution, the S might originate from impurities in the mesh and Cl turned out to come diffusing out of the Ag/AgCl reference electrode onto the $ZnCo_2O_4$ surface, making it unsuitable in highly alkaline solutions.

The high-purity mesh from Good fellow showed much better stability in 1 molar KOH (pH $\approx 13.8 - 14$), as shown in Fig. 5.12.

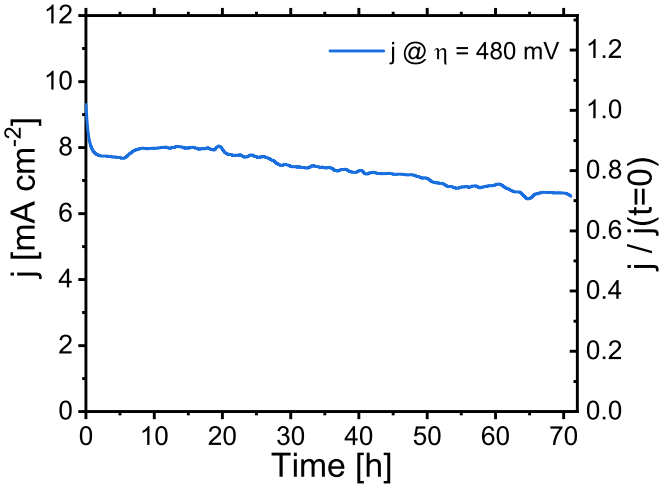

Figure 5.12.: Chronoamperometry measurement of a $ZnCo_2O_4$ sample on Ti-mesh after 1000 cycles.

The measurement was done after completing 1000 cycles (cf. section 5.3.1). A potential of $\eta = 480\,\mathrm{mV}$ equivalent to $1.71\,\mathrm{V}$ vs. RHE is applied. The initial current density yields around $9.2\,{}^{\mathrm{mA}}/_{\mathrm{cm}^2}$. During the measurement, the produced current remains approximately constant for 30 hours, before slowly dropping to around $6.5\,{}^{\mathrm{mA}}/_{\mathrm{cm}^2}$, corresponding to a drop of around 35% after almost another 73 hours of continuous operation.
This means that the $ZnCo_2O_4$ oxygen evolution catalyst is very stable and able to operate for 1000 cycles plus another 73 hours at an overpotential of $\eta = 480\,\mathrm{mV}$, producing a current density of around $6 - 9\,{}^{\mathrm{mA}}/_{\mathrm{cm}^2}$.

In summary, $ZnCo_2O_4$ acts as a highly active OER catalyst in alkaline solution with low overpotentials in the range of $390 - 470\,\mathrm{mV}$, low Tafel slopes of $56 - 103\,{}^{\mathrm{mV}}/_{\mathrm{dec}}$ comparable to literature and excellent long-term stability for almost 500 hours.

5.4. Photoelectrocatalytic Properties of $ZnCo_2O_4$

Even more attractive is the utilization of (sun)light as an additional external source of energy for the water splitting process. Semiconductors like $ZnCo_2O_4$ are potential candidates as photoelectrocatalysts due to the band gap. According to section 2.2, the generated charge carriers facilitate the water splitting reaction. Consequently, less electrical energy should be required to reach a certain reaction rate. The measurements are carried out the same way as before, except a flow cell is used instead of an H-cell. The cell and the tubes are carefully filled with 1M KOH, after being connected to the KOH container and the collecting vessel for the used electrolyte placed below the cell (cf. section 4.3.3).
This section discusses first results on the photoelectrocatalytic activity of $ZnCo_2O_4$ on 2%Al:ZnO samples under illumination with simulated sunlight (intensity: $100\,\mathrm{mW/cm^2}$). The $ZnCo_2O_4$ possesses a nominal thickness of 350 nm, absorbing most of the light of the sun simulator. The transparent 2%Al:ZnO is 300 nm thick.

5.4.1. Cyclic Voltammetry

Fig. 5.13 a) shows the cyclic voltammetry measurements (scan rate $50\,\mathrm{mV/s}$) of a $ZnCo_2O_4$/AZO sample in the 1M KOH flow cell with and without illumination. As before, the x- and y-axis, denote the RHE potential and the produced current. The top x-axis shows the overpotential $\eta = E - 1.23\,\mathrm{V}$ of the oxygen evolution reaction.

Since the shape of the CVs look similar to regular electrochemistry measurements, the flow cell is working properly, providing enough electrolyte to the catalyst surface and keeping ohmic losses small. In the flow cell setup, an overpotential of around $460\,\mathrm{mV}$ at $10\,\mathrm{mA/cm^2}$ is observed which is comparable to the results obtained in section 5.3. Moreover, the redox peaks are visible again at around $1.1\,\mathrm{V}$ and $1.5\,\mathrm{V}$ vs. RHE. However, the system seems to be not completely stable and therefore, no chronoamperometry stability tests have been performed. Already during cyclic voltammetry measurements without illumination with the solar simulator, the observed current drops with every cycle. Fig. 5.13 b) shows the measured cycles vs. time. The blue, dahsed vertical line indicates the moment where the solar simulator was turned on. As experienced in

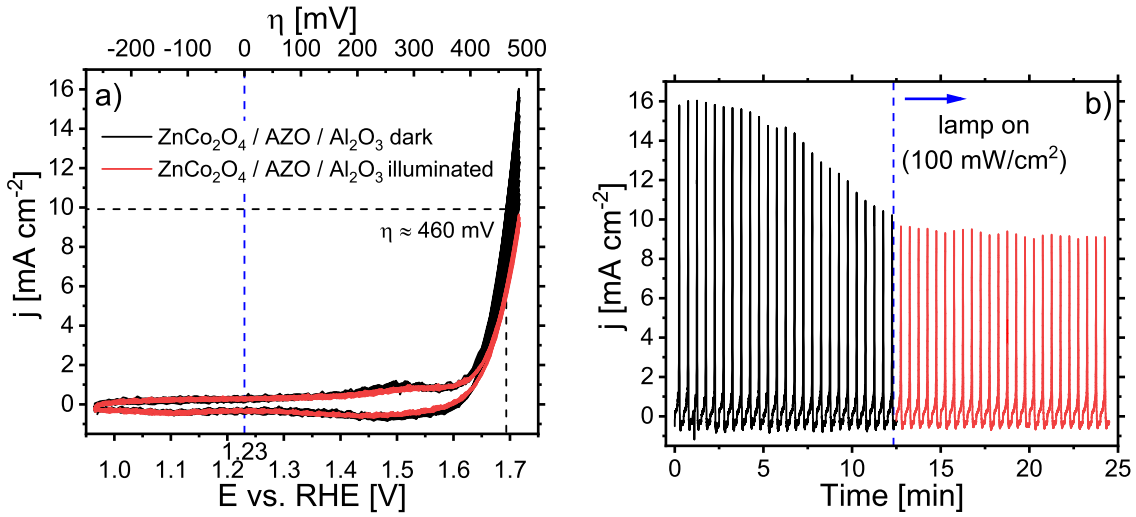

Figure 5.13.: Results of the photoelectrochemistry measurements: CVs with and without illumination (a) and the same cycles plotted versus time (b).

previous experiments, after some time the aggressive, highly alkaline electrolyte gets in contact with the AZO layer and starts to dissolve it due to the harsh oxidizing conditions. The Au capping layer does not stick to the AZO and $ZnCo_2O_4$ very well, and therefore tends to peel off from the layers beneath. As a consequence, the AZO along with the catalyst is removed from the sample. Thus, the expected facilitating effect of the photoelectrocatalysis could not be seen.

However, after turning on the lamp with an intensity of $100\,\mathrm{mW/cm^2}$, the degradation of the sample appears to be slowed down or even stopped. After dropping from around $16\,\mathrm{mA/cm^2}$ to $9\,\mathrm{mA/cm^2}$ without illumination, the current stabilizes at $\sim 9\,\mathrm{mA/cm^2}$ with the lamp turned on ($100\,\mathrm{mW/cm^2}$). This behaviour might be an indication of the photoelectrocatalytic activity of $ZnCo_2O_4$. In order to illucidate this assumption, further measurements with improved stability and protection of the catalyst and AZO surface should be done in the future, but were not in the time frame of this master thesis. Nevertheless, the flow cell is tight and operating correctly without additional ohmic resistances within the system. The flow of fresh electrolyte through the cell provides enough water molecules for the reaction and prevents accumulation of produces bubbles at the anode surface.

5.4.2. Tafel analysis

In order to obtain the Tafel slopes of the $ZnCo_2O_4$ samples used for the investigation of the photoelectrocatalytic activity, the same procedure as above is used. The oxygen evolution overpotential η is plotted vs. the produced current density j (on a logarithmic scale), according to section 2.4.

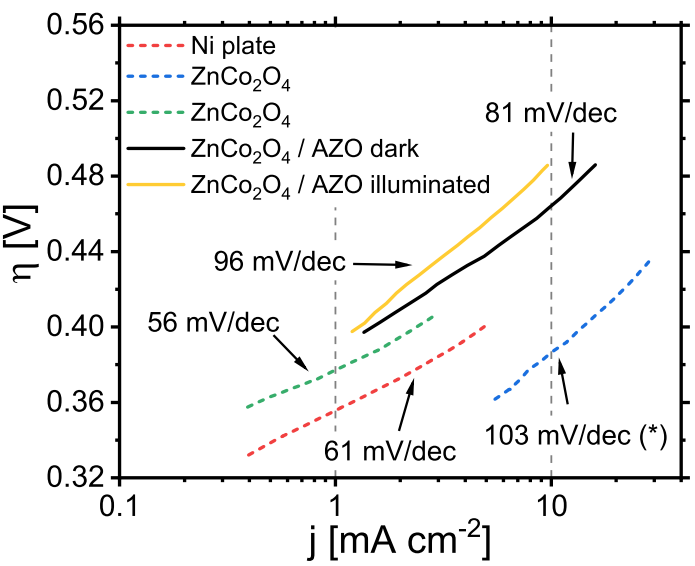

Figure 5.14.: Tafel plot of $ZnCo_2O_4$ / 2%Al:ZnO samples during photoelectrochemistry meaurements without (black) and with illumination of the electrode (yellow) in 1M KOH.

Fig. 5.9 depicts these Tafel plots for the $ZnCo_2O_4$ / 2%Al:ZnO samples in the flow cell with 1 molar KOH and for comparison, the Ni plate and the $ZnCo_2O_4$ / Ti-mesh samples (dashed). Tafel slopes of approximately $81\,^{\mathrm{mV}}/_{\mathrm{dec}}$ without and $96\,^{\mathrm{mV}}/_{\mathrm{dec}}$ with illumination in 1 molar KOH are determined. The values are in the region of the measurements done in the H-cell with $ZnCo_2O_4$ on the Ti-mesh. In fact, the Tafel slopes of the measurements lie between the $56\,^{\mathrm{mV}}/_{\mathrm{dec}}$ and $103\,^{\mathrm{mV}}/_{\mathrm{dec}}$ obtained for the $ZnCo_2O_4$ samples on the titanium meshs at around $1\,^{\mathrm{mA}}/_{\mathrm{cm^2}}$ and $10\,^{\mathrm{mA}}/_{\mathrm{cm^2}}$, respectively, Thus, it is concluded that the mass transfer kinetics of the water molecules to the catalyst surface in the flow cell are sufficiently fast enough with a flow rate of $\approx 0.4-0.5\,^{\mathrm{l}}/_{\mathrm{h}}$. The dark measurement exhibits both a lower overpotential and Tafel slope than the one with the sun simulator turned on. This is due to the fact that the catalyst/sample was degrading over time, reducing the efficiency of the reaction cycle by cycle.

In summary, $ZnCo_2O_4$ is observed to be a highly active oxygen evolution reaction catalyst, showing overpotentials in the range of $\eta = 390 - 470\,\mathrm{mV}$ at $10\,{}^{\mathrm{mA}}/_{\mathrm{cm}^2}$ with stability for almost 500 hours in 1M KOH, measured via cyclic voltammetry and chronoamperometry. Other, lower pH electrolytes, work as well, but higher overpotentials ($>$ 500 mV) are necessary. Titanium meshes are suitable as substrates, but their purity and cleanliness are very important. Tafel analysis indicates that the reaction kinetics are quite efficient with slopes of $56 - 103\,{}^{\mathrm{mV}}/_{\mathrm{dec}}$ close to Ni and previously reported values, depending on the current density range. The highly-transparent and conducting 2%Al:ZnO electrode allows measurments in a flow cell configuration despite some stability issues with 1 molar KOH aqueous solution. The cell is properly working, with efficient mass transfer and minimized ohmic losses, resulting in low Tafel slopes ($81 - 96\,{}^{\mathrm{mV}}/_{\mathrm{dec}}$) and overpotentials of approximately $460\,\mathrm{mV}$ in order to produce a current density of around $10\,{}^{\mathrm{mA}}/_{\mathrm{cm}^2}$.

6

Conclusion and Outlook

The work of this master thesis focuses on the electrocatalytical properties of $ZnCo_2O_4$ systems regarding the oxygen evolution reaction and presents first results of photoelectrocatalytic test experiments. The oxygen evolution reaction is kinetically hindered and therefore the limiting factor in water splitting to O_2 and H_2 [2]. For this study, two sample types and experimental setups are required. $ZnCo_2O_4$ on a titanium mesh serves as the sample type for electrochemistry measurements. The setup consists of an H-cell filled with electrolyte (1M potassium hydroxide or carbonates), a 1M KOH mercury/mercuric-oxide reference electrode and a Ni counter electrode. $ZnCo_2O_4$/ 2%Al:ZnO on c-sapphire is used for photoelectrochemistry. In order to be able to use the sun simulator with an intensity of $100\,{}^{\mathrm{mW}}/_{\mathrm{cm}^2}$, a flow cell type of setup had to be developed. Tubes connected to one container filled with the electrolyte and one empty collecting vessel allowed a flow rate of around $400 - 500\,{}^{\mathrm{ml}}/_{\mathrm{h}}$ through the cell. The CE consists of a Pt plate and the 1M KOH Hg/HgO reference electrode is used and connected via a short tube. In order to get an estimation of its standard electrode potential, calibration with respect to a 3M KCl Ag/AgCl electrode was done.

The samples were grown by physical vapor deposition methods, namely RMS and PLD. $ZnCo_2O_4$ is grown by RMS with a heater temperature of $T_{\mathrm{H}} = 665\,°\mathrm{C}$ and an Ar : O_2 ratio of $10 : 0.5$, whereas AZO is grown by PLD with a heater temperature of $T_{\mathrm{H}} = 600\,°\mathrm{C}$ and Ar : O_2 ratio of $10 : 1$. Concerning the crystal quality, $ZnCo_2O_4$ is assumed to grow in poor crystallinity and rather amorphous on the Ti-mesh. On the contrary, AZO grows excellently on sapphire, showing an intense Al:ZnO (002) peak at $2\theta = 34.41\,°$ (FWHM $= 0.35\,°$). $ZnCo_2O_4$ on sapphire and AZO mainly shows multiples of the cubic (111) reflections with the $ZnCo_2O_4$ (222) at $2\theta = 38.02\,°$ (FWHM $= 0.28\,°$), but also a small Co:ZnO (002) wurtzite phase impurity.

The chemical composition of the samples' surface is investigated by x-ray photoelectron

spectroscopy. The study confirms the bonding of Zn and Co to the O atoms on the surface of $ZnCo_2O_4$ on Ti-mesh. The L_3 and L_2 peaks of cobalt found at $E_B = -781\,eV$ and $E_B = -796\,eV$, respectively, with a satellite splitting of around $7 - 8\,eV$. The Zn 2p states are detected at binding energies of $-1044\,eV$ and $-1021\,eV$. Interestingly, Ti 2p peaks were only observed on a $ZnCo_2O_4$ sample with an intermediate titanum layer on sapphire. One reason for the non-existence of Ti peaks on $ZnCo_2O_4$ / Ti-mesh samples could be contamination during the fabrication processes (oil, fat,...) or during heat treatments. Auger electron spectroscopy analysis reveals that the initially bought Ti-mesh was contaminated with a thick layer of carbon and/or carbondioxide, possibly affecting the stability. But even after substrate cleaning and consecutive XPS measurements before and after the growth of $ZnCo_2O_4$ without breaking vacuum, Ti peaks remain absent.

The activity of $ZnCo_2O_4$ as an oxygen evolution reaction catalyst is demonstrated by electrochemistry measurements in different electrolytes. The mesh geometry of the substrate improves the mass-transfer of H_2O molecules to the catalyst surface. The plain titanium mesh showed no increase in reaction rates up to high potentials of more than $2\,V$ vs. RHE. When only 200 nm of $ZnCo_2O_4$ catalyst ar grown on it, the reaction rate increases significantly at lower voltages around $1.6 - 1.8\,V$ vs. RHE. In 1M potassium bicarbonate, potassium carbonate and potassium hydroxide (with increasing pH), the overpotentials (potential in addition to the thermodynamically predicted value) to generate a current density of $10\,{}^{mA}/_{cm^2}$ are 810 mV in 1M $KHCO_3$ and approximately $390 - 470\,mV$ in 1M KOH, comparable to reported values of the most efficient transition metal oxide catalysts [9]. First long-term measurements demonstrate the stability for around 150 hours. However, some instabilities are observed which can, for example, be related to impurities and dirt on the substrate causing the catalyst to degrade in alkaline solution. With a high-purity titanium mesh substrate, performance for almost 500 hours was observed, working efficiently for 1000 cycles (around 416 hours) and another 3 days of operation with constant applied potential, whereas for other catalysts, stability is oftenly only shown for a few days or hours [9, 11]. The experimental data proves that $ZnCo_2O_4$ acts as an efficient oxygen evolution catalyst and Ti is a suitable, conducting and inactive substrate.

Tafel analysis of the $ZnCo_2O_4$ samples indicates fast reaction kinetics on the electrode with Tafel slopes in the range of $56 - 103\,{}^{mV}/_{dec}$ 1 molar KOH, close to reported values of $46\,{}^{mV}/_{dec}$ [11].

First photoelectrocatalyis experiments with $ZnCo_2O_4$ reveal that the instability of 2%Al:ZnO in 1 molar KOH is the main obstacle in photoelectrochemical measurements. Thus, a thin protective layer of gold is evaporated onto the AZO. A properly working flow cell configuration and the activity of $ZnCo_2O_4$ with overpotentials of around $460\,\mathrm{mV}$ at $10\,{}^{\mathrm{mA}}/_{\mathrm{cm}^2}$ were demonstrated. Nevertheless, after some time the KOH lifts the Au film and begins to dissolve the transparent electrode, along with the $ZnCo_2O_4$. Consequently, no conclusive results on the behaviour of the catalyst under illumination with light were obtained. However, after turning on the sun simulator lamp, the degradation of the catalyst is slowed down to some degree. Possible explanations for the absence of an photoelectrocatalytical effect are that the produced photo carriers recombine before taking part in the oxygen evolution reaction, too little electrons are excited or the degradation of the electrode dominates the catalytical effect.

In the future, this behaviour needs to be studied in more detail in order to get a more thorough understanding of the processes at the electrode surface. Moreover, the promising electrical and optical properties of 2%Al:ZnO make it very attractive in such photoelectrochemistry measurements, despite the stability issues in KOH. Using a more adhesive Ti/Au or simply Ti capping layer could prevent the electrolyte to get in contact with the electrode more effectively. Additionally, the $ZnCo_2O_4$ / TiO_2 stack proposed in Ref. [4] could be investigated. The pn-heterojunction of the titanium and $ZnCo_2O_4$ might provide a barrier for holes boosting the photoelectrocatalytic activity and reducing photo carrier recombination. Moreover, the effect of the crystallinity of the $ZnCo_2O_4$ on the mesh could be examined more closely. The mesh geometry improves the kinetics of the reaction but might influence the activity of the catalyst compared to those grown on flat substrates. In that case, a rotating disc electrode might be employed. Additional research could be done by the investigation of other promising material compounds, for instance nickel iron or nickel cobalt oxides [9, 21].

A
Appendix

A.1. Intensity spectrum of the solar simulator

For the photoelectrochemical measurements a FYTRONICS FY 7000 Solar Simulator was used. The intensity distribution is shown in Fig A.1. The measured spectrum[1] is cut off at around 900 nm due to the detection limit of the silicon diode used for data acquisition.

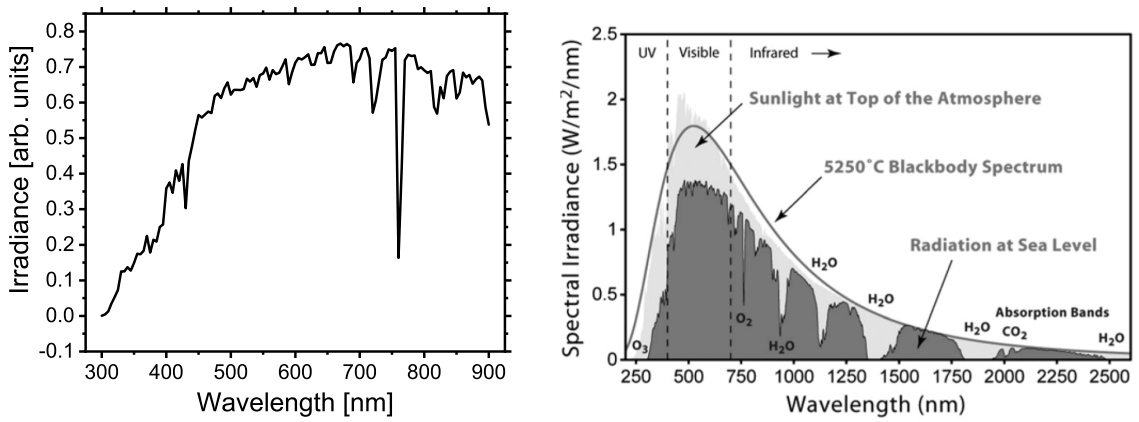

Figure A.1.: Measured spectrum of the solar simulator (a) and solar spectrum of our sun for comparison (taken from [68]) (b).

A.2. C++ program to reduce data points

During long-term experiments, very often several hundred thousand data points are taken by the potentiostat. Because it is not necessary to have data points every millisecond if

[1] Measurement done by Dr. Philipp Stadler

the measurement lasts several weeks, a short and simple C++ code has been developed to copy every n-th line of the data (in a text format) to a new file:

```
#include <iostream>
#include <string>
#include <fstream>
using namespace std;

int main()
{
//names of input and output files
std::ifstream infile("C:/Users/*name of file*.asc");
std::ofstream outfile("C:/*name of new file*.asc");
std::string line;

int count = 0;
while (getline(infile, line)) {       //scan file
int gap = 101;        //reduction factor + 1

      if (count % gap == 0) {       //write line to new file
outfile « line « std::endl;
count++;
}
count++;
}

cout « "Lines successfully copied to output file!" « endl;
cout « "Press any key to close." « endl;
outfile.close();
infile.close();
getchar();
return 0;
}
```

Bibliography

[1] S.J. Smith, J. Edmonds, C.A. Hartin, A. Mundra, and K. Calvin. *Near-term acceleration in the rate of temperature change*. *Nature Climate Change*, **5**:333–336, 2015. doi: 10.1038/nclimate2552.

[2] Z.W. Seh, J. Kibsgaard, C.F. Dickens, I. Chorkendorff, J.K. Nørskov, and T.F. Jaramillo. *Combining theory and experiment in electrocatalysis: Insights into materials design*. *Science*, **355**(6321), 2017. ISSN 0036-8075. doi: 10.1126/science.aad4998.

[3] I. Roger, M.A. Shipman, and M.D. Symes. *Earth-abundant catalysts for electrochemical and photoelectrochemical water splitting*. *Nature Reviews Chemistry*, **1**, 01 2017. doi: 10.1155/2013/196521. article Nr.: 0003.

[4] A. Sarkar, K. Karmakar, and G.G. Khan. *Designing Co-Pi Modified One-Dimensional n-p $TiO_2/ZnCo_2O_4$ Nanoheterostructure Photoanode with Reduced Electron-Hole Pair Recombination and Excellent Photoconversion Efficiency (>3%)*. *J. Phys. Chem.*, **121**:25705–25717, 2017. doi: 10.1021/acs.jpcc.7b08213.

[5] C. Jiang, S.J.A. Moniz, A. Wang, T. Zhang, and J. Tang. *Photoelectrochemical devices for solar water splitting - materials and challenges*. *Chem. Soc. Rev.*, **46**:4645, 2017. doi: 10.1039/c6cs00306k.

[6] A. Fujishima and K. Honda. *Electrochemical Photolysis of Water at a Semiconductor Electrode*. *Nature*, **238**:37–38, 1972. doi: 10.1038/238037a0.

[7] N. Koshida and Y. Kiuchi. *Observation of a Long-Life Photoelectrochemical Conversion withn-Type Porous-Si Photoelectrodes*. *Japanese Journal of Applied Physics*, **4**(3):L166–L168, 1985. doi: 10.1143/jjap.24.l166.

[8] L.C. Seitz, C.F. Dickens, K. Nishio, Y. Hikita, J. Montoya, A. Doyle, C. Kirk, A. Vojvodic, H.Y. Hwang, J.K. Norskov, and T.F. Jaramillo. *A highly active and stable $IrO_x/SrIrO_3$ catalyst for the oxygen evolution reaction*. *Science*, **353**(6303):1011–1014, 2016. ISSN 0036-8075. doi: 10.1126/science.aaf5050.

[9] C.C.L. McCrory, S. Jung, J.C. Peters, and T.F. Jaramillo. *Benchmarking Heterogeneous Electrocatalysts for the Oxygen Evolution Reaction*. *J. Am. Chem. Soc.*, **135**, 2013. doi: 10.1021/ja407115p.

[10] M. Chauhan, K.P. Reddy, C.S. Gopinath, and S. Deka. *Copper Cobalt Sulfide Nanosheets Realizing a Promising Electrocatalytic Oxygen Evolution Reaction*. *ACS Catal.*, **7**:5871–5879, 2017. doi: 10.1021/acscatal.7b01831.

[11] T.W. Kim, M.A. Woo, M. Regis, and K. Choi. *Electrochemical Synthesis of Spinel Type $ZnCo_2O_4$ Electrodes for Use as Oxygen Evolution Reaction Catalysts*. *J. Phys. Chem. Lett.*, **5**:2370–2374, 2014. doi: 10.1021/jz501077.

[12] T. Liu, Y. Liang, Q. Liu, X. Sun, Y. He, and A.M. Asiri. *Electrodeposition of cobalt-sulfide nanosheets film as an efficient electrocatalyst for oxygen evolution reaction*. *Electrochemistry Communications*, **60**:92–95, 2015. doi: 10.1016/j.elecom.2015.08.011.

[13] S. Han, S. Liu, R. Wang, X. Liu, L. Bai, and Z. He. *One-Step Electrodeposition of Nanocrystalline $Zn_xCo_{3-x}O_4$ Films with High Activity and Stability for Electrocatalytic Oxygen Evolution*. *App. Mater. Interfaces*, **9**:17189–17194, 2017. doi: 10.1021/acsami.7b04841.

[14] Bo Zhang, Xueli Zheng, Oleksandr Voznyy, Riccardo Comin, Michal Bajdich, Max García-Melchor, Lili Han, Jixian Xu, Min Liu, Lirong Zheng, F. Pelayo García de Arquer, C.T. Dinh, et al. *Homogeneously dispersed multimetal oxygen-evolving catalysts*. *Science*, **352**(6283):333–337, 2016. doi: 10.1126/science.aaf1525.

[15] C.E. Housecroft and A.G. Sharpe. *Inorganic Chemistry*. Pearson Education Limited 2001, 4^{th} edition, 2012. ISBN 978-0-273-74278-4.

[16] A.J. Bard and L.R. Faulkner. *Electrochemical Methods: Fundamentals and Applications*. John Wiley and Sons, Inc., 2^{nd} edition, 2001.

[17] J.M. Thomas and W.J. Thomas. *Principles and Practice of Heterogeneous Catalysis*. Wiley-VCH Verlag GmbH & Co Germany 2015, 2^{nd} edition, 2015. ISBN 978-3-527-31458-4.

[18] K. Liu, X. Li, L. Liang, J. Wu, X. Jiao, J. Xu, Y. Sun, and Y. Xie. *Ni-doped $ZnCo_2O_4$ atomic layers to boost the selectivity in solar-driven reduction of CO_2*. *Nano Research*, **11**(6):2897–2908, 2018. doi: 10.1007/s12274-017-1943-2.

[19] S. Wang, Z. Ding, and X. Wang. *A stable $ZnCo_2O_4$ cocatalyst for photocatalytic CO_2 reduction*. *Chem. Commun.*, **51**:1517–1159, 2015. doi: 10.1039/c4cc07225a.

[20] M. Prasad, V. Sharma, A. Rokade, and S. Jadkar. Photoelectrochemical cell: A versatile device for sustainable hydrogen production. In N.D. Sankir and M. Sankir, editors, *Photo-Electrochemical Solar Cells*, pages 59–120. Scrivener Publishing and John Wiley & Sons, 2019. ISBN 9781119459934.

[21] V. Vij, S. Sultan, A.M. Harzandi, A. Meena, J.N. Tiwari, W.-G. Lee, Y. Yoon, and K.S. Sim. *Nickel-Based Electrocatalysts for Energy-Related Applications: Oxygen Reduction, Oxygen Evolution, and Hydrogen Evolution Reactions*. *ACS Catal.*, **7**: 7196–7225, 2017. doi: 10.1021/acscatal.7b01800.

[22] I.C. Man, H.-Y. Su, F. Calle-Vallejo, H.A. Hansen, J.I. Martínez, N.G. Inoglu, J. Kitchin, T.F. Jaramillo, J.K. Nørskov, and J. Rossmeisl. *Universality in Oxygen Evolution Electrocatalysis on Oxide Surfaces*. *ChemCatChem*, **3**:1159–1165, 2011. doi: 10.1002/cctc.201000397.

[23] M.G. Walter, E.L. Warren, J.R. McKone, S.W. Boettcher, Q. Mi, E.A. Santori, and N.S. Lewis. *Solar Water Splitting Cells*. *Chem. Rev.*, **110**(11):6446–6473, 2010. doi: 10.1021/cr1002326.

[24] M. Ciobanu, J.P. Wilburn, M.L. Krim, and D.E. Cliffel. Fundamentals. In Cynthia G. Zoski, editor, *Handbook of Electrochemistry*, pages 3 – 29. Elsevier, Amsterdam, 2007. ISBN 978-0-444-51958-0. doi: https://doi.org/10.1016/B978-044451958-0.50002-1.

[25] M.D. Arning and S.D Minteer. Electrode potentials. In Cynthia G. Zoski, editor, *Handbook of Electrochemistry*, pages 813 – 827. Elsevier, Amsterdam, 2007. ISBN 978-0-444-51958-0. doi: https://doi.org/10.1016/B978-044451958-0.50035-5.

[26] P.R. Roberge. *Corrosion Engineering Principles and Practice*. The McGraw-Hill Companies, 2008. ISBN 13-978-0071482431. doi: 10.1036/0071482431.

[27] T. Shinagawa, A.T. Garcia-Esparza, and K. Takanabe. *Insight on Tafel slopes from a microkinetic analysis of aqueous electrocatalysis for energy conversion*. *Scientific Reports*, **5**:13801, 2015. doi: 10.1038/srep13801.

[28] S. Kim, C. Ahn, Y. Cho, G. Hyun, S. Jeon, and J.H. Park. *Suppressing buoyant forces: New avenue for long-term durability of oxygen evolution catalysts*. *Nano Energy*, **54**:184–191, 2018. doi: 10.1016/j.nanoen.2018.10.009.

[29] T.J. Smith and K.J. Stevenson. Reference electrodes. In Cynthia G. Zoski, editor, *Handbook of Electrochemistry*, pages 73–110. Elsevier, Amsterdam, 2007. ISBN 978-0-444-51958-0. doi: https://doi.org/10.1016/B978-044451958-0.50002-1.

[30] S. Szabó and I. Bakos. *Reference Electrodes in Metal Corrosion*. *International Journal of Corrosion*, **2010**, 2010. doi: 10.1155/2010/756950.

[31] JKU Linz HLF Institute. *X-Ray diffraction from a Semiconductor Heterostructure*. Anleitung zum Fortgeschrittenenpraktikum, WS 2017/18.

[32] R. Gross and A. Marx. *Festkörperphysik*. Walter de Gruyter GmbH, Berlin/Boston, 2^{nd} edition, 2014. ISBN 978-3-11-035869-8.

[33] Ruppweb Org. URL `https://www.ruppweb.org/Xray/tutorial/spcdiff.htm`. Accessed on: 26.11.2019.

[34] S. Hüfner. *Photoelectron Spectroscopy: Principles and Applications*. Springer-Verlag Berlin Heidelberg GmbH, 3^{rd} edition, 2003. doi: 10.1007/978-3-662-09280-4.

[35] S. Hofmann. *Auger- and X-Ray Photoelectron Spectroscopy in Materials Science: A User-Oriented Guide*. Springer-Verlag Berlin Heidelberg GmbH, 2013. doi: 10.1007/978-3-642-27381-0.

[36] J.F. Watts and J. Wolstenholme. *An inroduction to Surface Analysis by XPS and AES*. John Wiley & Sons Ltd 2003, 2003. ISBN 9780470847121. doi: 10.1002/0470867930.

[37] Ü. Özgür, Y.I. Alivov, A. Teke, M.A. Reshchikov, S. Doğan, V. Avrutin, S.-J. Cho, and H. Morkoç. *A comprehensive study of ZnO materials and devices*. *J. Appl. Phys.*, **98**:041301, 2005. doi: 10.1063/1.1992666.

[38] M. Buchner, B. Henne, V. Ney, J. Lumetzberger, F. Wilhelm, A. Rogalev, A. Hen, and A. Ney. *Pinned orbital moments in uncompensated antiferromagnetic Co doped ZnO*. *J. Appl. Phys.*, **123**:203905, 2018. doi: 10.1063/1.5023898.

[39] M. Buchner, B. Henne, V. Ney, and A. Ney. *Transition from a hysteresis-like to an exchange-bias-like responseof an uncompensated antiferromagnet*. *Phys. Rev. B*, **99**:064409, 2019. doi: 10.1103/PhysRevB.99.064409.

[40] R.K. Shukla, A. Srivastava, A. Srivastava, and K.C. Dubey. *Growth of transparent conducting nanocrystalline Al doped ZnO thin films by pulsed laser deposition*. *Journal of Crystal Growth*, **294**:427–431, 2006. doi: 10.1016/j.jcrysgro.2006.06.035.

[41] B. Henne, V. Ney, K. Ollefs, F. Wilhelm, A. Rogalev, and A. Ney. *Magnetic interactions in theZn-Co-O system: tuning local structure, valence and carrier type from extremely Co doped ZnO to $ZnCo_2O_4$. Sci. Rep.*, **5**:16863, 2015. doi: 10.1038/srep16863.

[42] C. Ai, M. Yin, C. Wang, and J. Sun. *Synthesis and characterization of spinel type $ZnCo_2O_4$ as a novel anode material for lithium ion batteries*. *Journal of Materials Science*, **39**:1077–1079, 2004. doi: 10.1023/B:JMSC.0000012948.27433.83.

[43] T. Huang, C. Zhao, R. Zheng, Y. Zhang, and Z. Hu. *Facilely synthesized porous $ZnCo_2O_4$ rodlike nanostructure for high-rate supercapacitors*. *Ionics*, **21**:3109–3115, 2015. doi: 10.1007/s11581-015-1491-2.

[44] M. Gusenbauer. *All-Oxide Solar Cells*. *Master thesis*, 2019.

[45] Y. Liu, Y. Li, and H. Zeng. *ZnO-Based Transparent Conductive Thin Films: Doping, Performance, and Processing*. *Jornal of Nanomaterials*, **2013**, 2013. doi: 10.1155/2013/196521. article ID: 196521.

[46] M. Stoica and C. S. Lo. *P-type zinc oxide spinels: application to transparent conductors and spintronics*. *New Jornal of Physics*, **16**:055011, 2014. doi: doi: 10.1088/1367-2630/16/5/055011.

[47] Y. Shi, P.F. Ndione, L.Y. Lim, D. Sokaras, T. Weng, A.R. Nagaraja, A.G. Karydas, J.D. Perkins, T.O. Mason, D.S. Ginley, A. Zunger, and M.F. Toney. *Self-doping and electrical conductivity in spinel oxides: experimental validation of doping rules*. *Chem. Mater.*, **26**(5):1867, 2014. doi: 10.1021/cm404031k.

[48] J.D. Perkins, T.R. Paudel, A. Zakutayew, P.F. Ndione, P.A. Parilla, D.L. Young, S. Lany, D.S. Ginley, A. Zunger, N.H. Perry, Y. Tang, M. Grayson, T.O. Mason, J.S. Bettinger, Y. Shi, and M.F. Toney. *Inverse design approach to hole doping in ternary oxides: Enhancing p-type conductivity in cobalt oxide spinels*. *Phys. Rev. B*, **84**:205207, 2011. doi: 10.1103/PhysRevB.84.205207.

[49] M.N. Amini, H. Dixit, R. Saniz, D. Lamoen, and B. Partoens. *The origin of p-type conductivity in ZnM_2O_4 (M=Co,Rh,Ir) spinels*. *Phys. Chem. Chem. Phys.*, **16**: 2588–2596, 2014. doi: 10.1039/c3cp53926a.

[50] H.J. Kim, I.C. Song, J.H. Sim, H. Kim, D. Kim, Y.E. Ihm, and W.K. Choo. *Electrical and magnetic properties of spinel-type magnetic semiconductor ZnCo2O4 grown by reactive magnetron sputtering*. *J. Appl. Phys.*, **95**:7378, 2004. doi: 10.1063/1.1688571.

[51] B. Henne. *Structure, valence and magnetism of the Zn-Co-O system above the coalescene limit: From Wurtzite Co:ZnO to the $ZnCo_2O_4$ spinel*. *PhD thesis*, 2017.

[52] J. Lumetzberger. *Growth, structural and magnetic properties of Zn/Al doped nickel ferrite*. *Master thesis*, 10 2018.

[53] GESTIS-Stoffdatenbank of the IFA. URL `http://gestis.itrust.de/nxt/gateway.dll/gestis_de/002090.xml?f=templates$fn=default.htm$3.0`. Accessed on: 26.09.2019.

[54] H. Sun, H. Takahashi, N. Nishiumi, Y. Kamada, K. Sato, K. Nedu, Y. Matsushima, A. Khosla, M. Kawakami, H. Furukawa, P. Stadler, and T. Yoshida. *Vanadium Redox Flow Batteries Fabricated by 3D Printing and Employing Recycled Vanadium Collected from Ammonia Slag*. *J. of the Electrochem. Soc.*, **116**(9):B3125–B3130, 2019. doi: 10.1149/2.0251909jes.

[55] MaterialsProject, . URL `https://materialsproject.org/`. material ID: mp-46 (Titanium, Point group: 6/mmm). Accessed on: 26.11.2019.

[56] D.A.H. Hanaor and C.C. Sorrell. *Review of the anatase to rutile phase transformation*. *J. Mater. Sci.*, **46**:855–874, 2011. doi: 10.1007/s10853-010-5113-0.

[57] K. Thamaphat, P. Limsuwan, and B. Ngotawornchai. *Phase Characterization of TiO_2 Powder by XRD and TEM*. *Kasetsart J. (Nat. Sci.)*, **24**:357–361, 2008.

[58] V. V. Andreeva. *Behavior and nature of thin oxide films on some metals in gaseous media and in electrolyte solutions*. *Corrosion - National Association Of Corrosion Engineers*, **20**(2):35t–46t, 1964. doi: 10.5006/0010-9312-20.2.35t.

[59] MaterialsProject, . URL `https://materialsproject.org/`. material ID: mp-19275 (CoO, Point group: I4/mmm, Accessed on: 27.11.2019.

[60] D. Thompson, A. Attwood, E. Gullikson, M. Howells, K.-J. Kim, J. Kirz, J. Kortright, I. Lindau, Pianetta P., et al. *X-RAY DATA BOOKLET*. Lawrence Berkeley National Laboratory, 2^{nd} edition, January 2001.

[61] M. Oku and K. Hirokawa. *X-ray photoelectron spectroscopy of Co_3O_4, Fe_3O_4, Mn_3O_4 and related compounds*. *Journal of Electron Spectroscopy and Related Phenomena*, **8**:475–481, 1976.

[62] thermo scientific XPS. URL `https://xpssimplified.com/periodictable.php`. Accessed on: 02.12.2019.

[63] Materials Property Data MatWeb. URL `www.matweb.com/index.aspx`. Accessed on: 04.02.2020.

[64] Good Fellow. URL `http://www.goodfellow.com/`. Accessed on: 16.01.2020.

[65] A.R. Zeradjanin, A.A. Topalov, Q. Van Overmeere, S. Cherevko, X. Chen, E. Ventosa, W. Schuhman, and K.J.J. Mayrhofer. *Rational design of the electrode morphology for oxygen evolution – enhancing the performance for catalytic water oxidation*. *RSC Adv.*, **4**:9579–9587, 2014. doi: $10.1039/\mathrm{c3ra45998e}$.

[66] J. Oudar. *Sulfur Adsorption and Poisoning of Metallic Catalysts*. *Catalysis Reviews*, **22**(2):171–195, 1980. doi: $10.1080/03602458008066533$.

[67] D. Malko, T. Lopes, E. Symianakis, and A.R. Kucernak. *The intriguing poison tolerance of non-precious metal oxygen reduction reaction (ORR) catalysts*. *J. Mater. Chem. A.*, **4**:142–152, 2016. doi: $10.1039/\mathrm{C5TA05794A}$.

[68] M. Pagliaro, G. Palmisano, and R. Ciriminna. *Flexible Solar Cells*. Wiley-VCH Verlag GmbH & Co. KGaA, Weinheim, 2008. ISBN 978-3-527-32375-3.

Acknowledgements

I would like to express my sincere gratitude to the solid state physics division of the Johannes Kepler University Linz, especially Prof. Andreas Ney and his work group for the opportunity to do my master thesis under his supervision. I really enjoy the working environment and positive mentality of its members. All of them are happy to thoroughly discuss problems encountered and results obtained during the work.

Special thanks also to Dr. Philipp Stadler and Prof. Niyazi Serdar Sariçiftçi, for collaborating with the magnetic oxides group and providing the laboratories and equipment for the electrochemistry measurements. Dr. Stadler's and his work group's expertise helped me a lot and explained the rather new world of chemistry to me.

From the magnetic oxides group, I would especially like to thank Dr.^{in} Verena Ney for supporting me throughout this work and her help at the growth chamber. Also, many thanks to Julia, Santa and Martin who always tried to answer questions I had and shared their knowledge, and to Antonia and Markus for their help during chamber openings and following wrapping.

Last but not least I would like to thank all my friends who were always ready to mentally support me during hard exam preparation weeks and to my colleagues Lisa, Alex, Daniel and Michael with who I certainly spent weeks solving and discussing exercise sheets.

Vielen, vielen Dank an euch alle!